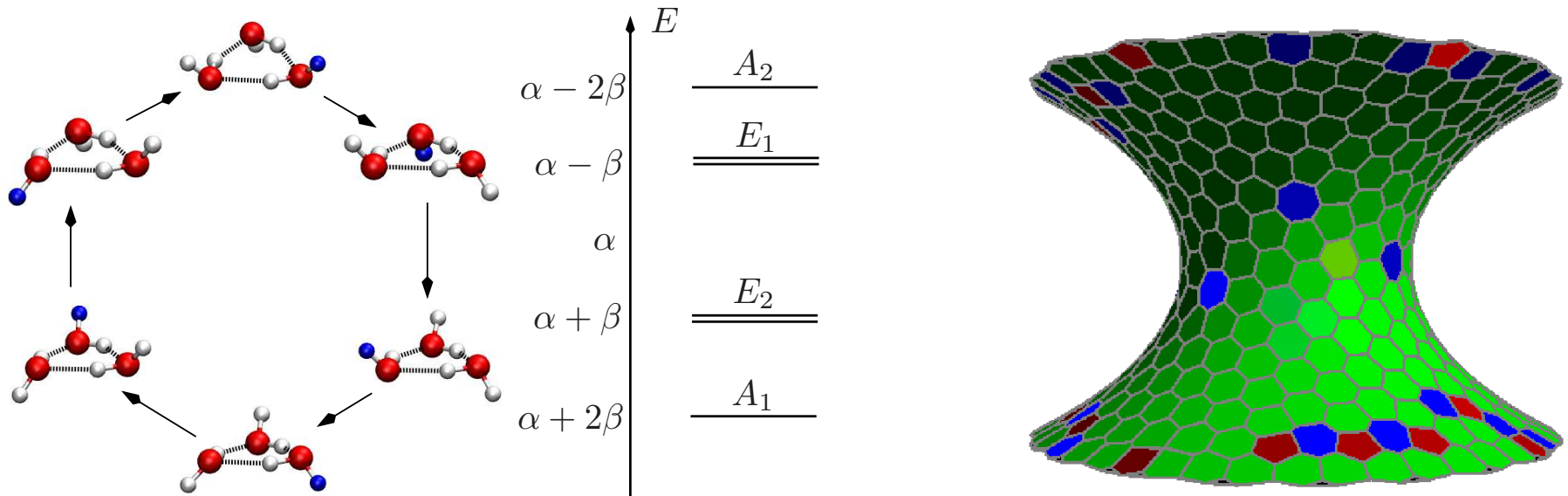


Energy Landscapes: Molecules, Nanodevices and Machine Learning

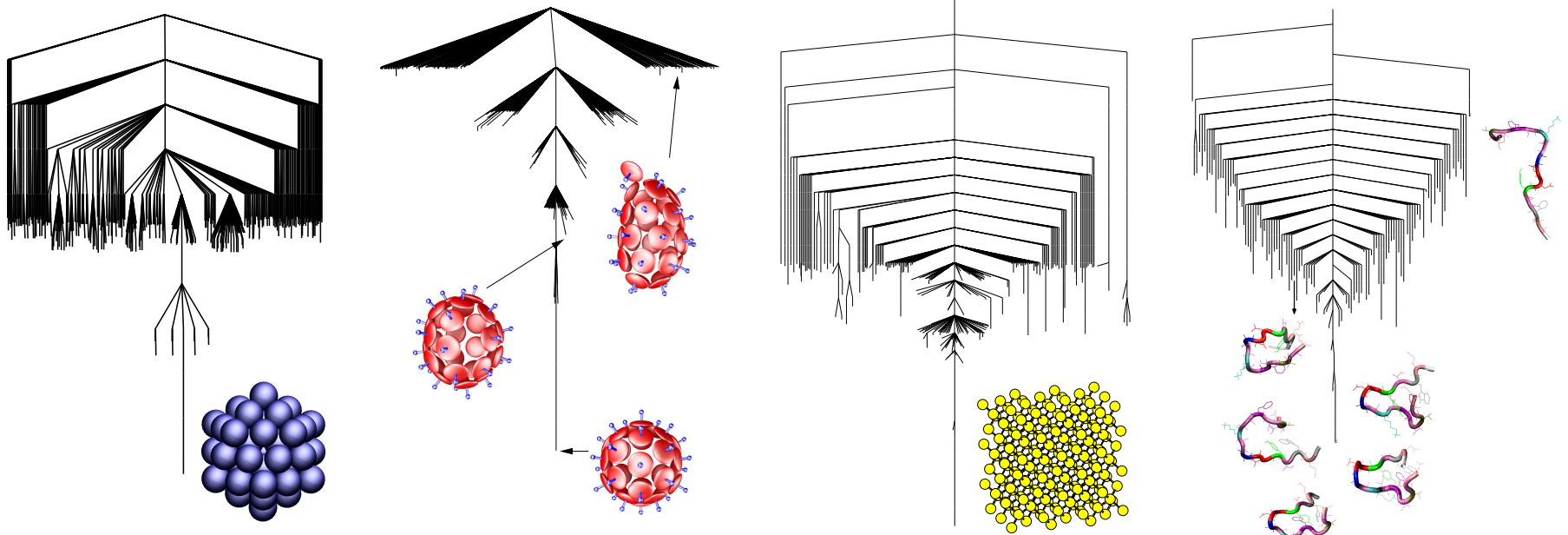
The potential energy **landscape**, defined by local **minima** and connecting **transition states**, is our **computational** and **conceptual** tool (*JPCB*, **110**, 20765, 2006):

- **Basin-hopping** for global optimisation (*J. Phys. Chem. A*, **101**, 5111 1997)
- **Basin-sampling** for global thermodynamics (*J. Chem. Phys.*, **124**, 044102, 2006)
- **Discrete path sampling** for (rare event) dynamics (*Mol. Phys.*, **100**, 3285, 2002)

For small molecules (**left**), all the relevant **stationary points** and **pathways** can be located. Larger systems (**right**) require appropriate **sampling**.

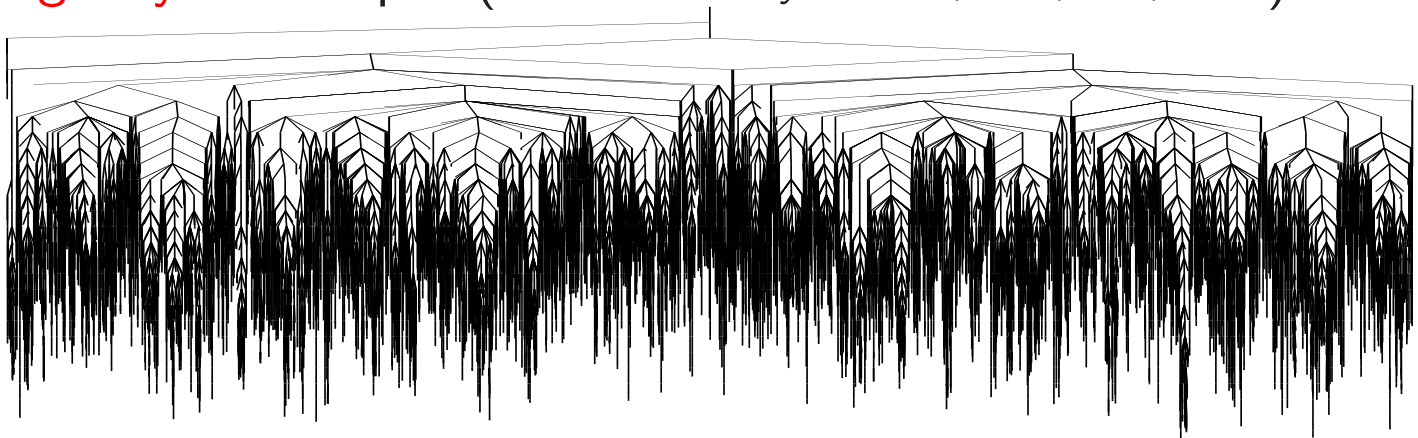


Self-Organisation is Encoded in Single Funnel Landscapes

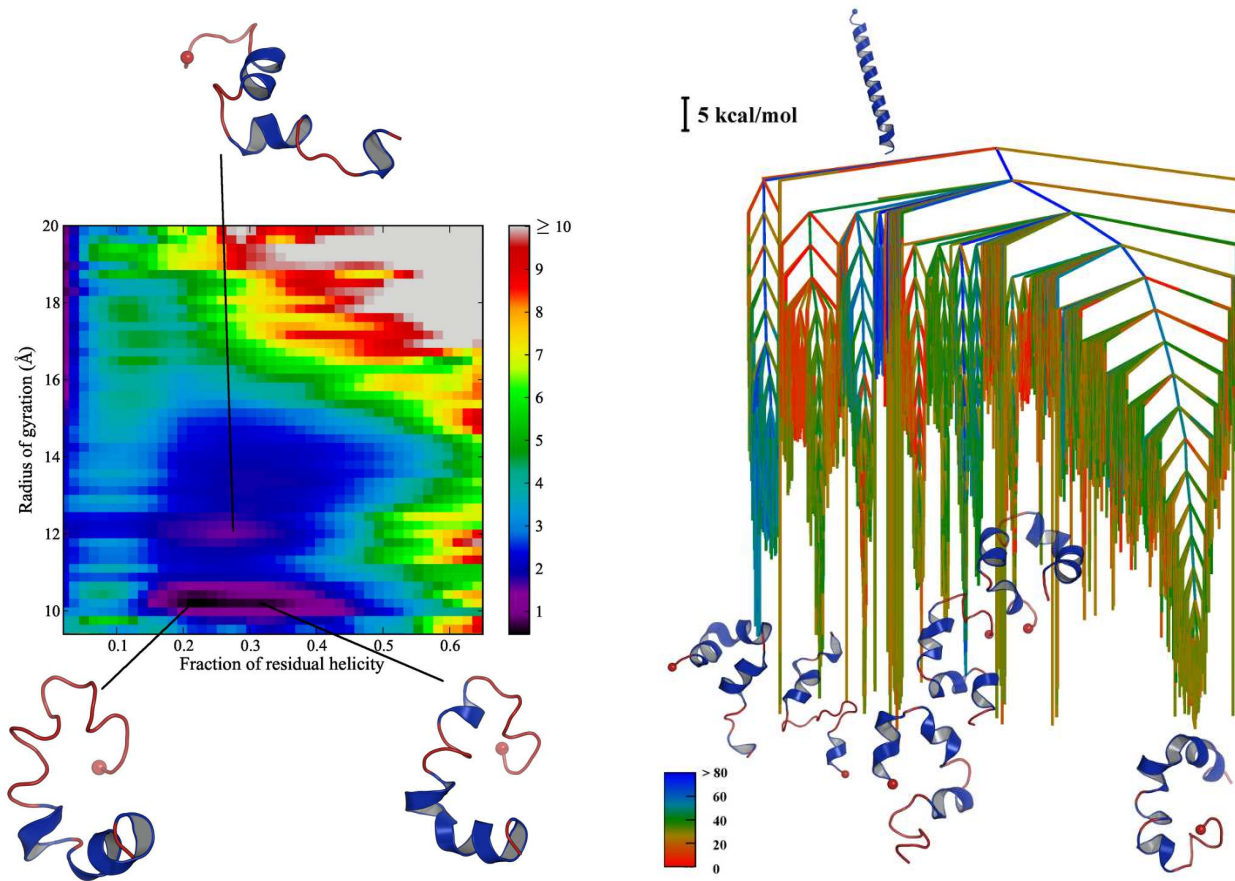


(Above) Energy landscapes for systems with **self-organising** properties. The **LJ₅₅ cluster**, an icosahedral **shell**, crystalline **silicon**, and the GB1 **peptide**.

(Below) A **glassy** landscape. (*Phil. Trans. Roy. Soc. A*, **363**, 357, 2005).



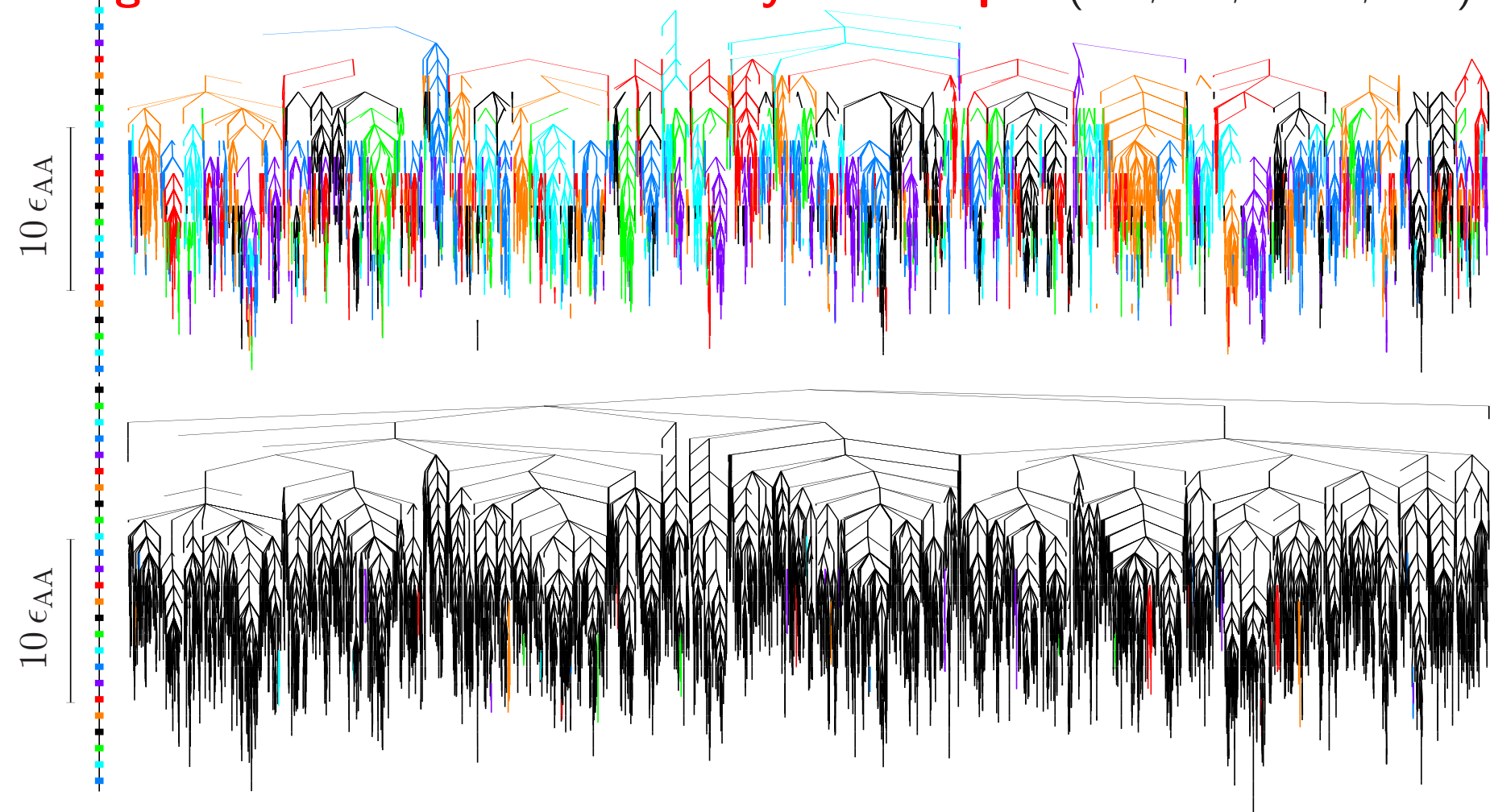
Multifunnel Landscapes May Encode Multifunctional Systems



The **intrinsically disordered** p53 upregulated modulator of apoptosis protein, has an **intrinsically multifunnel** landscape, consistent with **induced fit**.

Left: free energy surface at 280 K. **Right:** potential energy **disconnectivity graph** coloured according to the **α -helical** content. (*Sci. Rep.*, **5**, 10386, 2015)

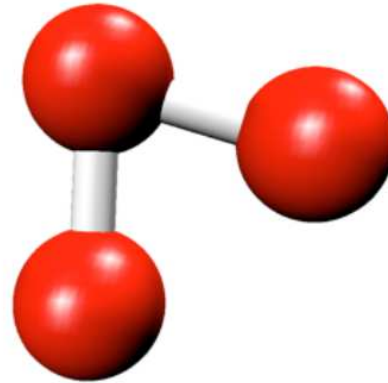
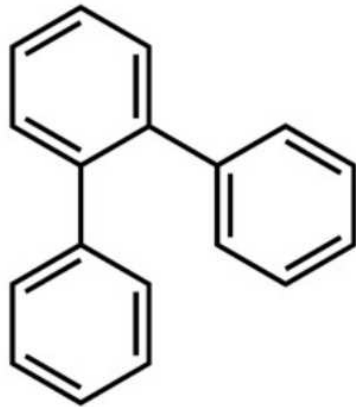
Higher Order Structure in Glassy Landscapes (*JCP*, 129, 164507, 2008)



Disconnectivity graphs for **BLJ₆₀** including only transition states for **noncage-breaking** (top) and **cage-breaking** (bottom) paths. Changes in colour indicate **disjoint** sets of minima. Cage-breaking transitions, defined by **two** nearest-neighbour changes, define a higher order **metabasin** structure.

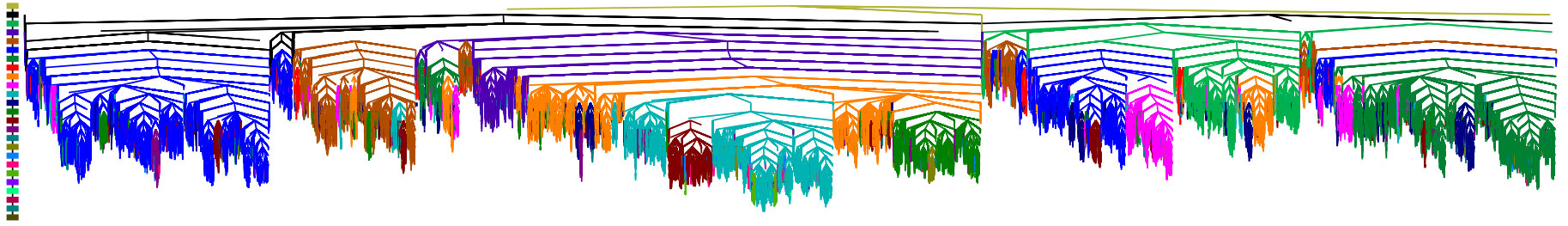
Diffusion in a Molecular Glass Former (*JCP*, **145**, 024505, 2016)

Lewis-Wahnstrom model for *ortho*-terphenyl: rigid body with the rings represented by *single* Lennard-Jones sites. These simulations employed **324** molecules with *periodic* boundary conditions.

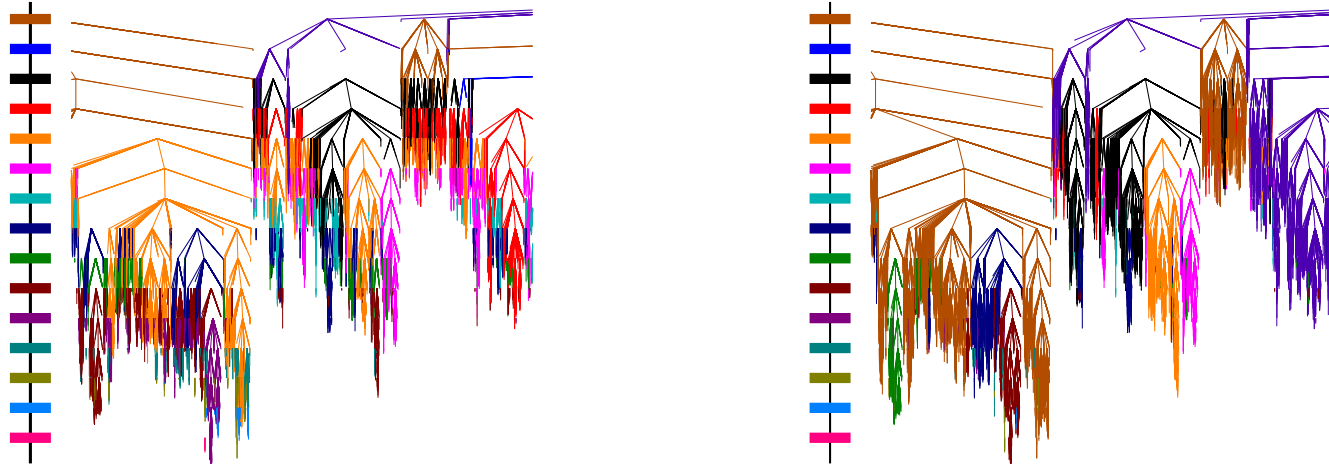


Analysis of *diffusion* in terms of *cage-breaking* rearrangements has been generalised from binary Lennard-Jones systems to this *molecular* glass former.

As for the atomic system, the cage-breaking pathways are *sufficient* to reproduce the correct *diffusion* constant.



Disconnectivity graph coloured according to the energy at which fragments are **separated** by **productive** cage breaks, defining **metabasin** structure.



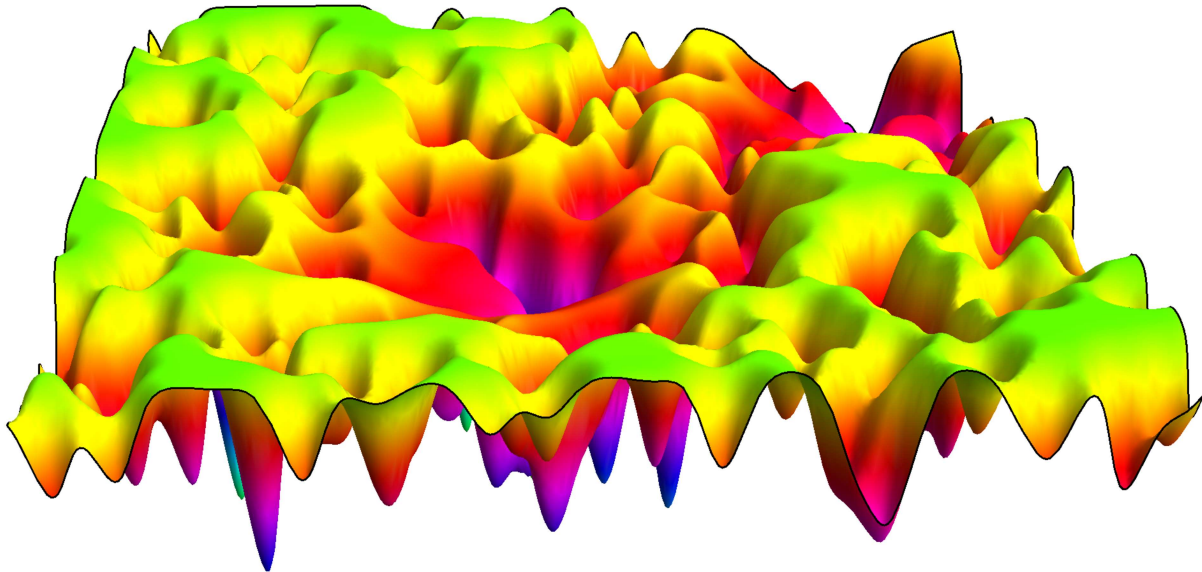
Magnified disconnection graphs coloured according to regions defined by **all** cage-breaks (left) and **productive** cage-breaks (right).

Super-Arrhenius behaviour is due to **negative correlations** in particle displacements defined over successive time windows.

Growth in the Number of Stationary Points

For m weakly coupled subsystems of $N/m = n$ atoms each the number of local minima satisfies $f_{\min}(mn) = f_{\min}(n)^m$, so that $f_{\min}(N) = e^{\alpha N}$. For transition states we expect $f_{\text{ts}}(mn) = m f_{\min}(n)^{m-1} f_{\text{ts}}(n)$ and hence $f_{\text{ts}}(N) = N e^{\alpha N} = N f_{\min}(N)$. (*Science*, **225**, **983**, 1984; *JCP*, **119**, 12409, 2003)

- Low-dimensional **projections** of the landscape can only represent the **connectivity** faithfully for a **few** anharmonic degrees of freedom.



Frustrated low-dimensional landscapes are **not** representative.

The Ring-Polymer Instanton Approach (*JCP*, **131**, 214106, 2009)

The **ring polymer** approximation to the quantum partition function $Q(\beta) = \text{trace} \left[e^{-\beta \hat{H}} \right]$ is obtained by a **Trotter** factorisation into P imaginary time steps of length $\beta \hbar / P$. For particles of mass m_j and $\mathbf{X} = \{\mathbf{X}_1, \dots, \mathbf{X}_P\}$:

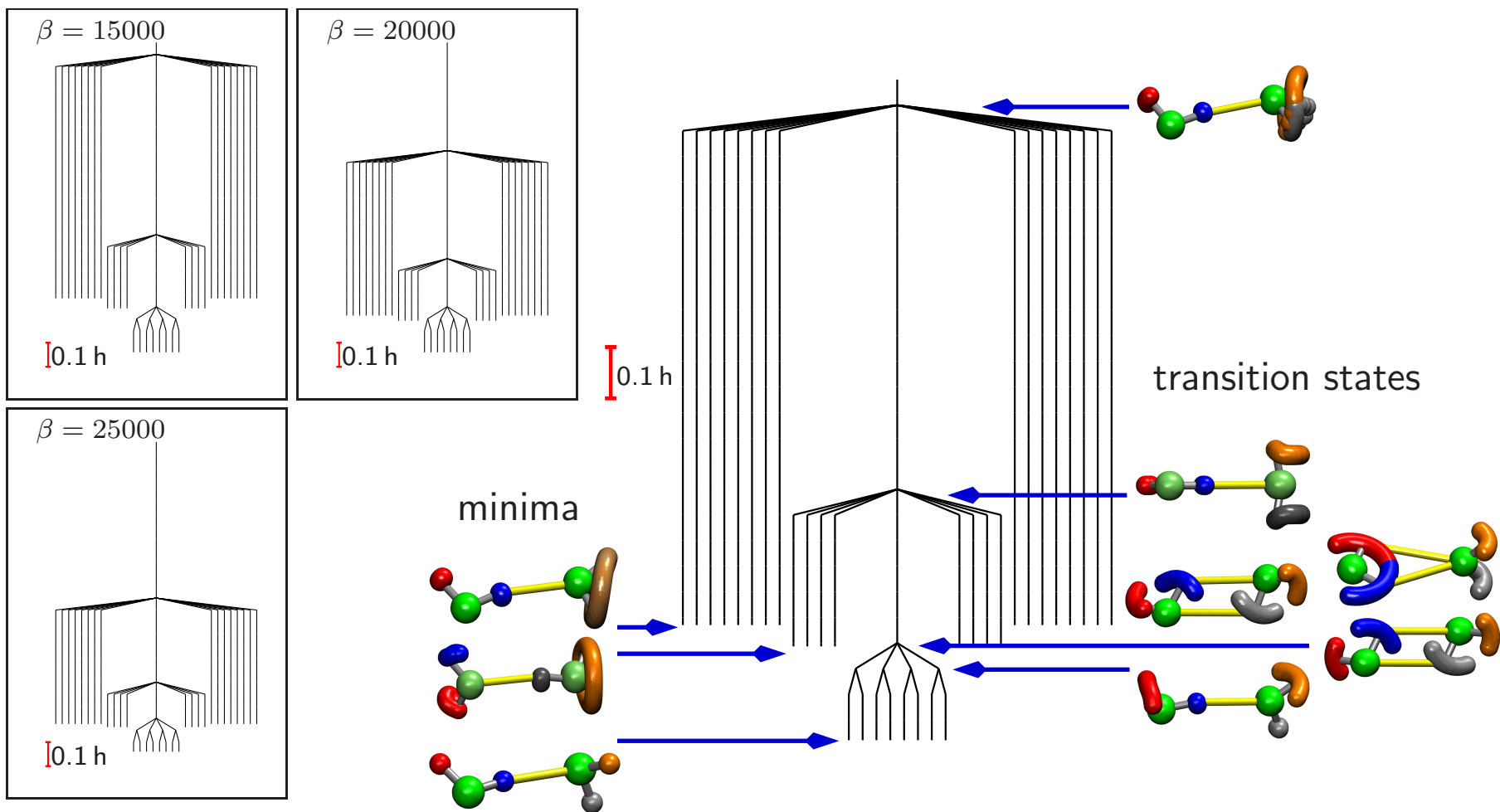
$$Q(\beta) \approx \left(\frac{mP}{2\pi\beta\hbar^2} \right)^{P/2} \int e^{-\beta U_P(\beta, \mathbf{X})/P} d\mathbf{X},$$

$$\text{with } U_P = \sum_{\alpha=1}^P \left[\sum_{j=1}^{3N} \frac{m_j P^2}{2\beta^2 \hbar^2} \left(X_{\alpha}^{(j)} - X_{\alpha+1}^{(j)} \right)^2 + V(\mathbf{X}_{\alpha}) \right],$$

a mapping onto a classical **ring polymer** with P beads, each corresponding to a configuration of the physical system and coupled by **harmonic springs**.

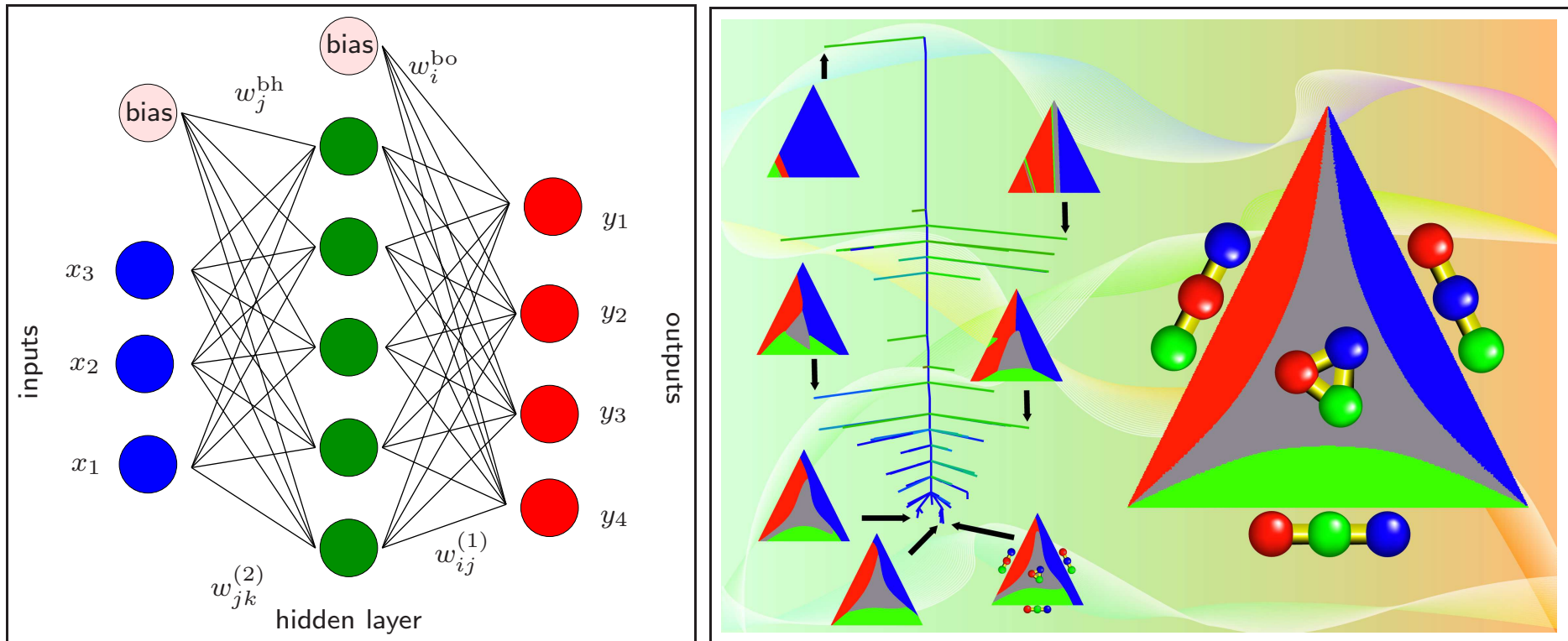
Transition states of $U_P(\beta, \mathbf{X})$ represent a finite-difference approximation to periodic **instanton** pathways. This approach provides approximate **tunneling splittings** with **all** degrees of freedom treated **quantum mechanically**.

Path Integral Energy Landscapes for Water Dimer



The ring polymer **landscape** of $(\text{H}_2\text{O})_2$ includes **classical** and **delocalised** minima and transition states for the **MBPOL** potential (results for 201 beads).

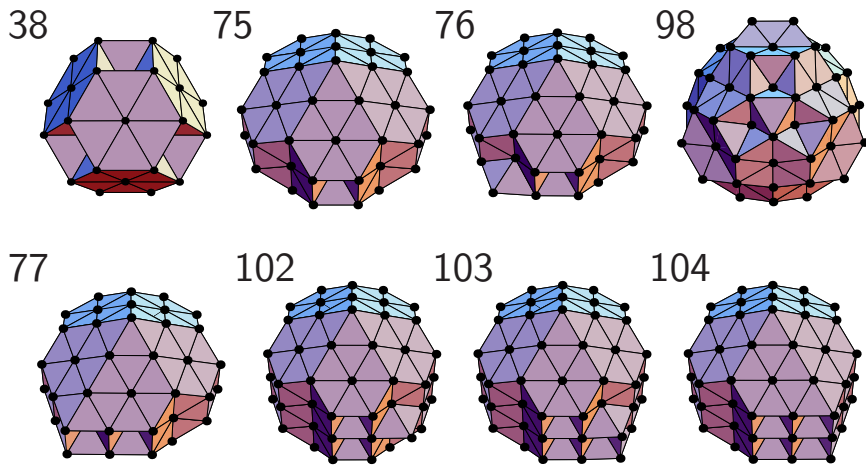
Machine Learning Landscapes (*JCP*, **144**, 124119, 2016; *CPL*, **667**, 158, 2017)



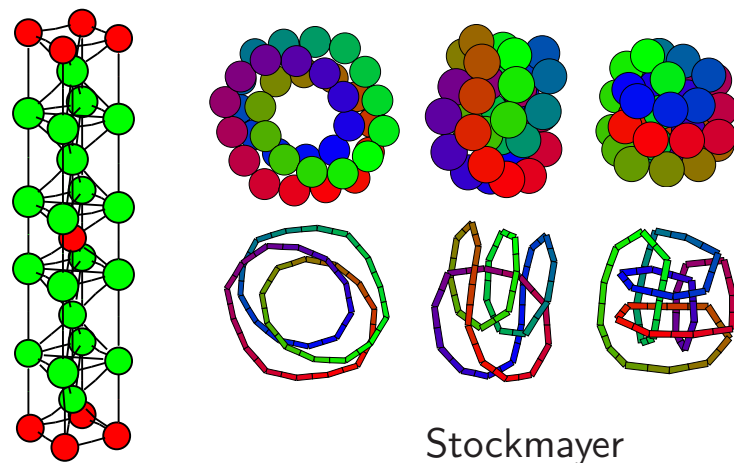
Neural network fits produce multiple solutions, defining a **landscape** for stationary points of the **cost function** for **multinomial logistic regression**.

In this example we predict the outcome of **geometry optimisation** for an **atomic cluster** with four distinct **isomers** using only the three initial **bond lengths**.

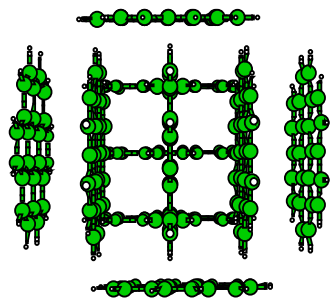
Basin-Hopping Global Optimisation (*J. Phys. Chem. A*, 101, 5111, 1997)



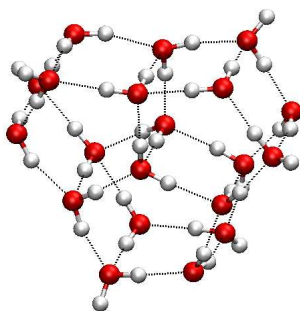
Non-icosahedral Lennard-Jones Clusters



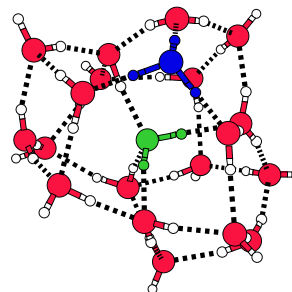
Binary LJ unit cell



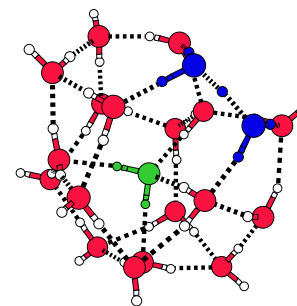
coronene₁₀



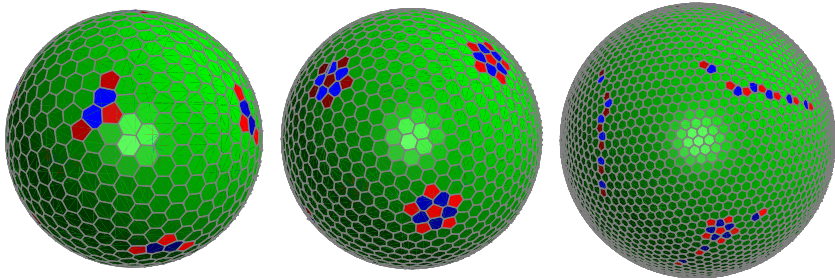
(H₂O)₂₀



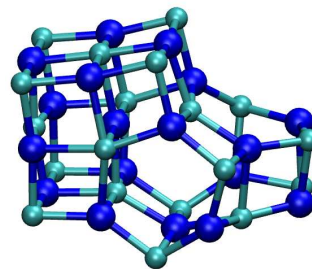
H₃O⁺(H₂O)₂₀ Eigen



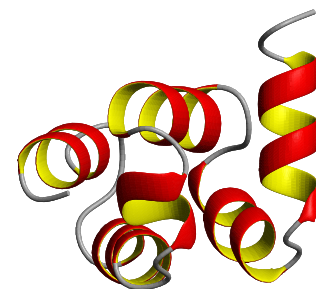
H₃O⁺(H₂O)₂₀ Zundel



Thomson problem



(NaCl)₁₈Na⁺



HYPA/FBP11

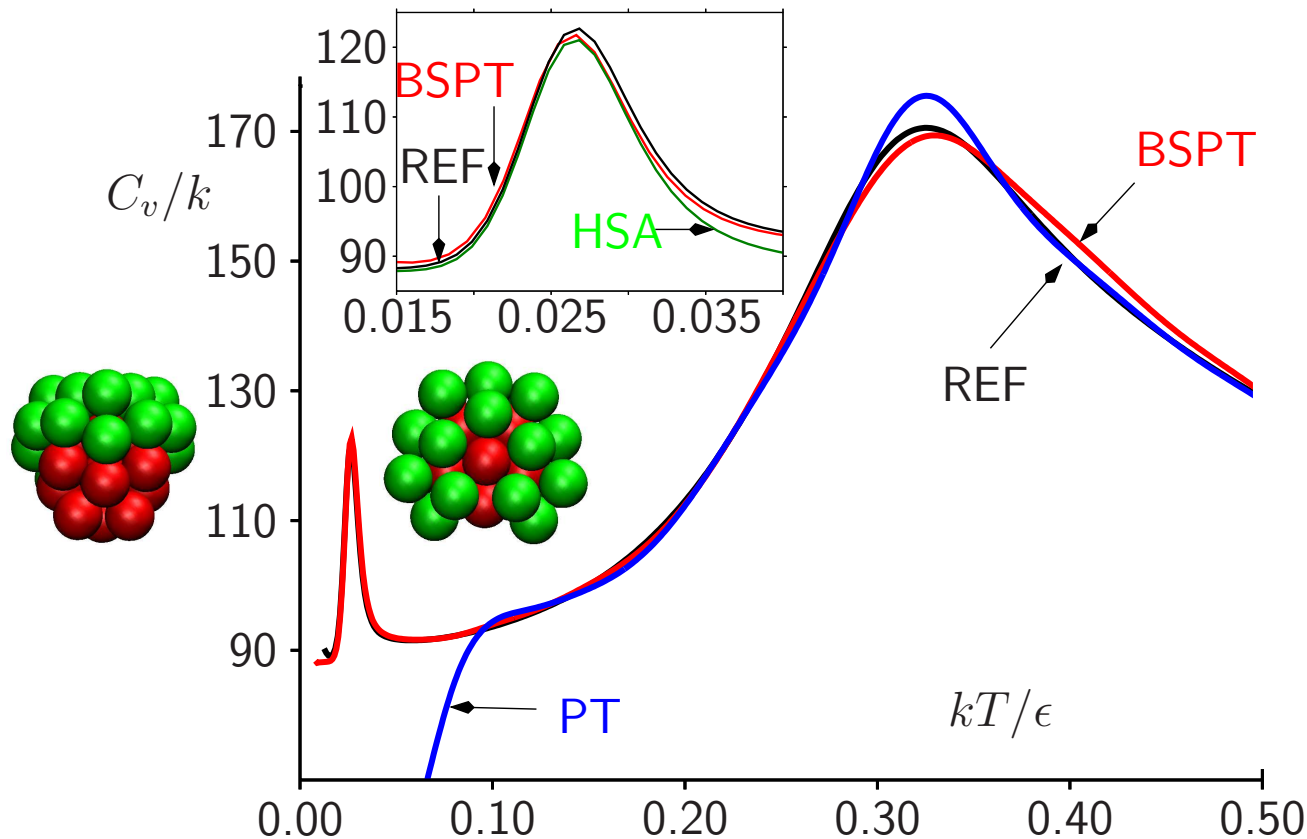
Basin-Sampling for Global Thermodynamics (*CPL*, 584, 1, 2013)

Broken ergodicity is treated using basin-hopping, while the configuration space corresponding to high temperature is sampled by parallel tempering.

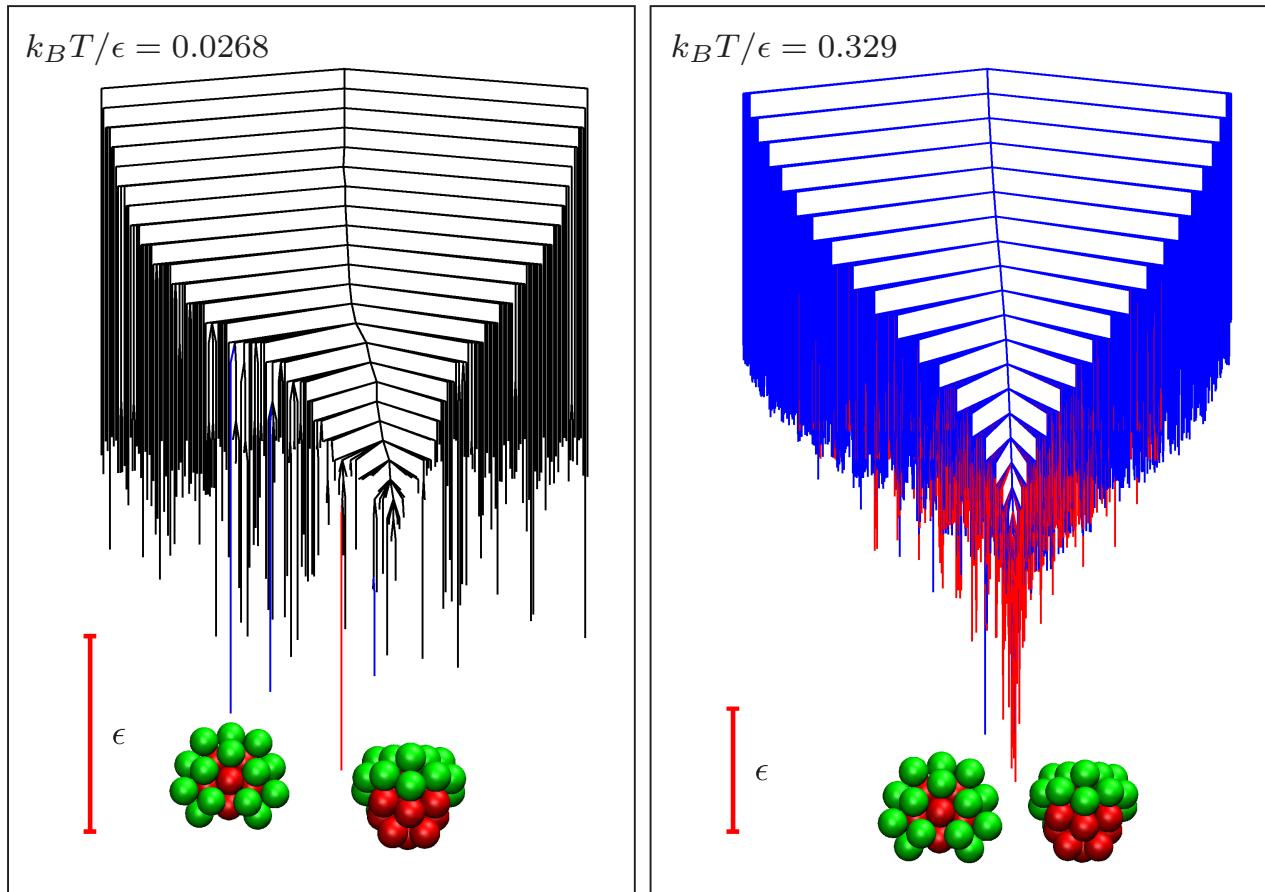
A two-dimensional anharmonic form is used to combine the density of states.

Accurate thermodynamics were obtained for the solid-solid phase transition in LJ_{31} in 21.8 minutes compared to 110.5 hours for parallel tempering.

in LJ_{31} in 21.8 minutes compared to 110.5 hours for parallel tempering.

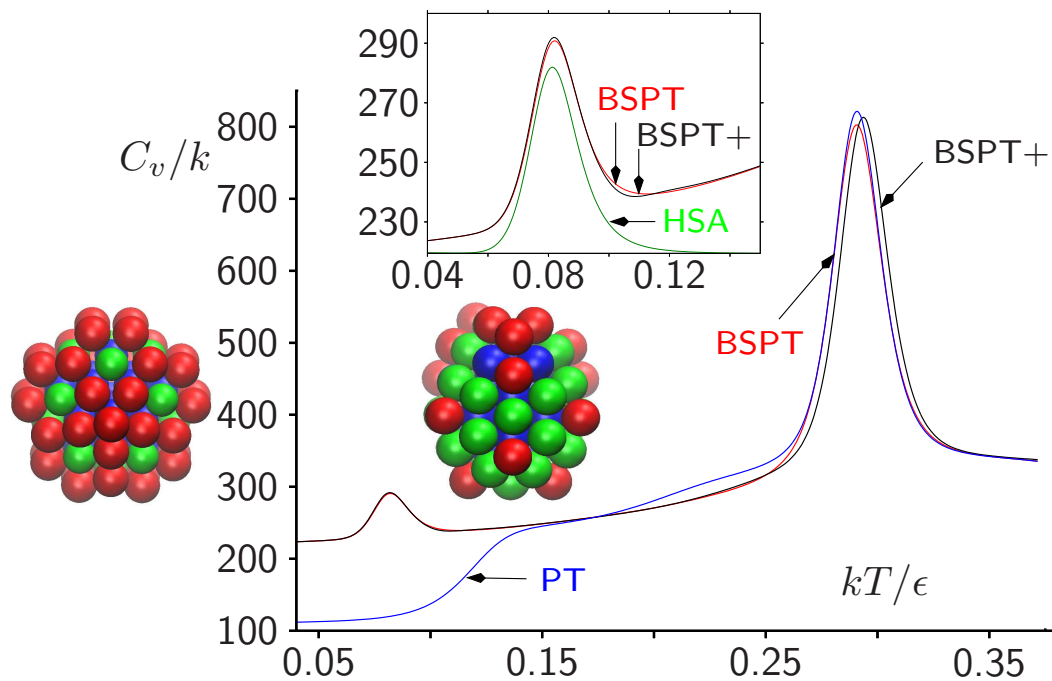
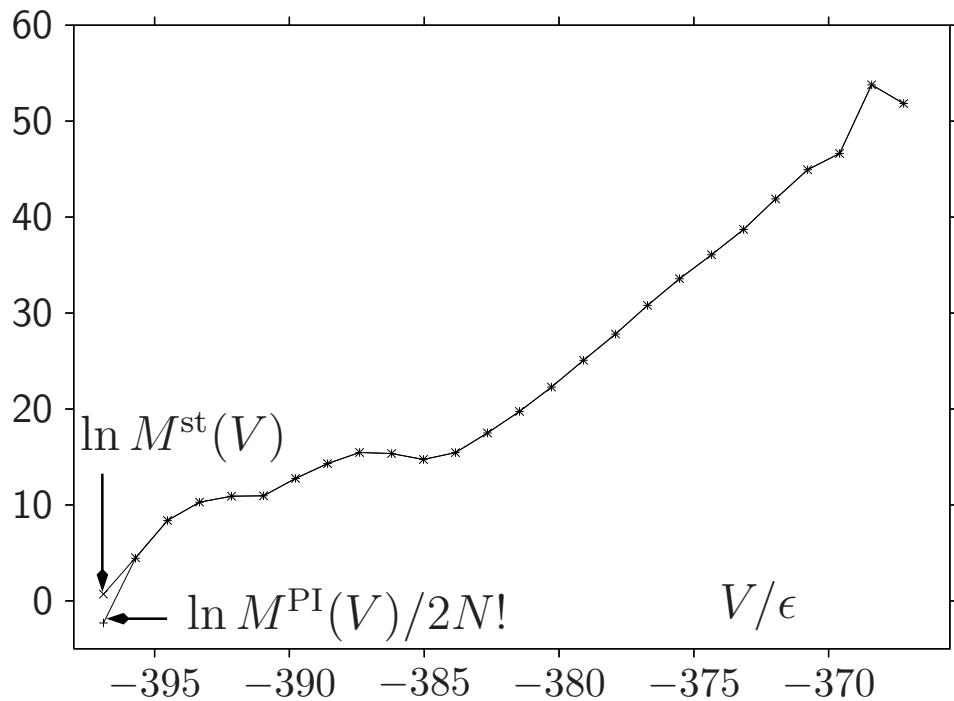


Assigning Heat Capacity Features (*Phys. Rev. E*, **95**, 030105R, 2017)

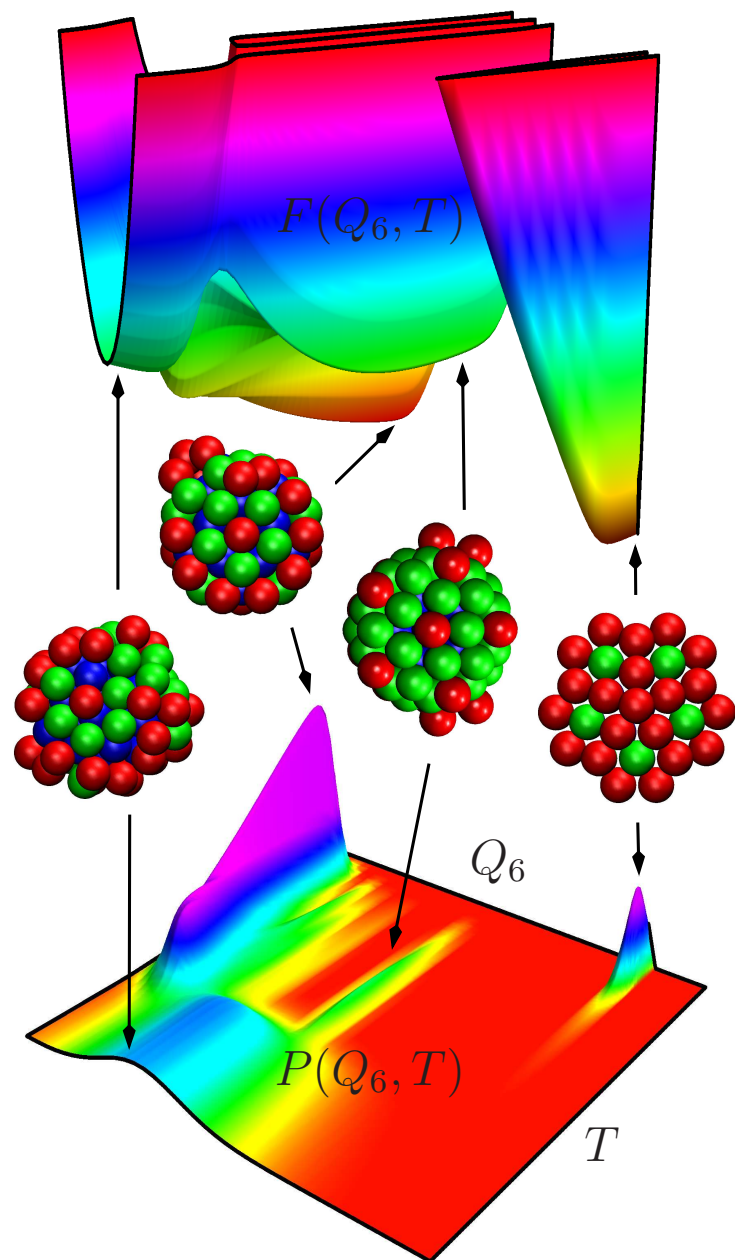


Contributions to C_V can be decomposed as sums over local minima with **positive** and **negative** occupation probability gradients, $g_\gamma(T) = \partial p_\gamma(T) / \partial T$:

$$C_V = \kappa k_B + k_B T^2 \sum_{\gamma}^{g_\gamma(T) > 0} g_\gamma(T)^2 / p_\gamma(T) + k_B T^2 \sum_{\gamma}^{g_\gamma(T) < 0} g_\gamma(T)^2 / p_\gamma(T)$$



Results for LJ₇₅



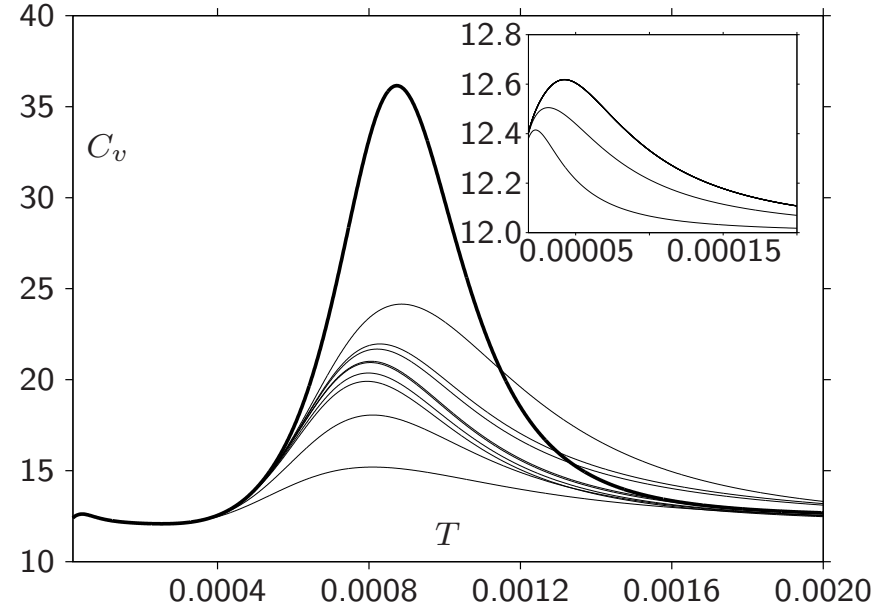
Machine Learning Healthcare Applications

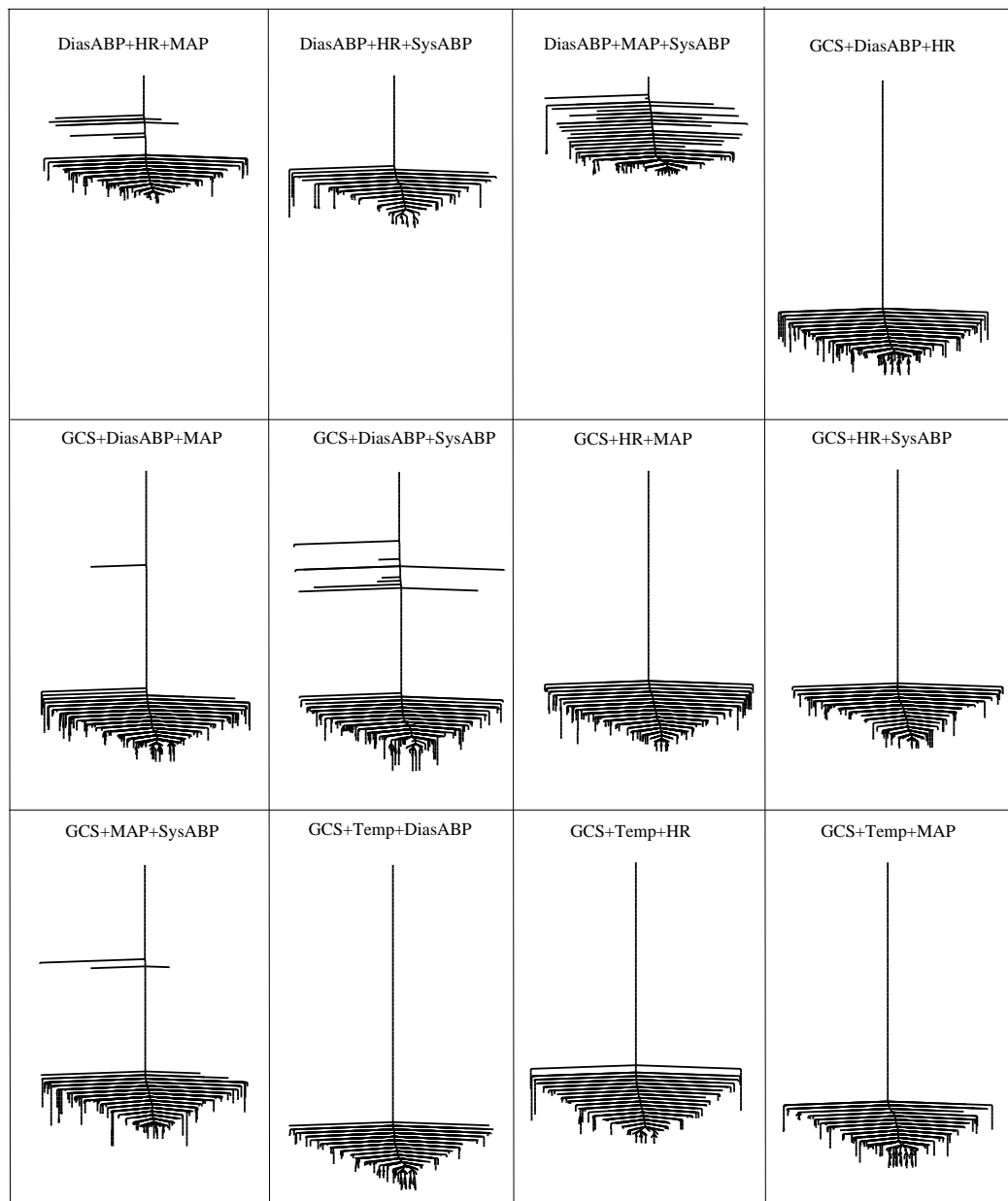
Sepsis prediction using the InSight package produced an AUC value of 0.8799 ± 0.0056 for MIMIC-III data. (*JMIR Med. Inform.*, **4**, e28, 2016)

Prediction of unplanned ICU readmission using an ensemble scheme based on MIMIC-III data achieved an AUC of **0.71**. (*BMJ Open*, **7**, e017199, 2017)

Perspective: *Phys. Chem. Chem. Phys.*, **19**, 12585–12603, 2017.

Our most systematic tests are for patient outcomes for MIMIC-II and MIMIC-III data, comparing the landscapes for neural network fits with different combinations of input data. The heat capacity analogue often exhibits multiple peaks. Can we construct better predictions?

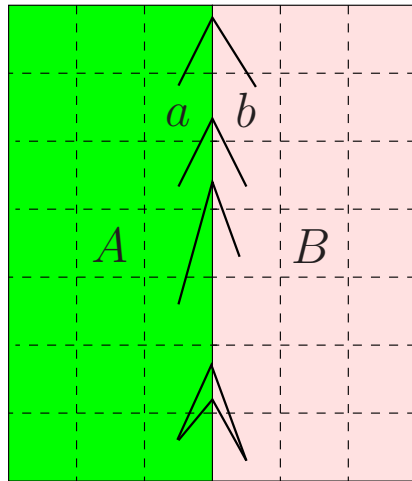




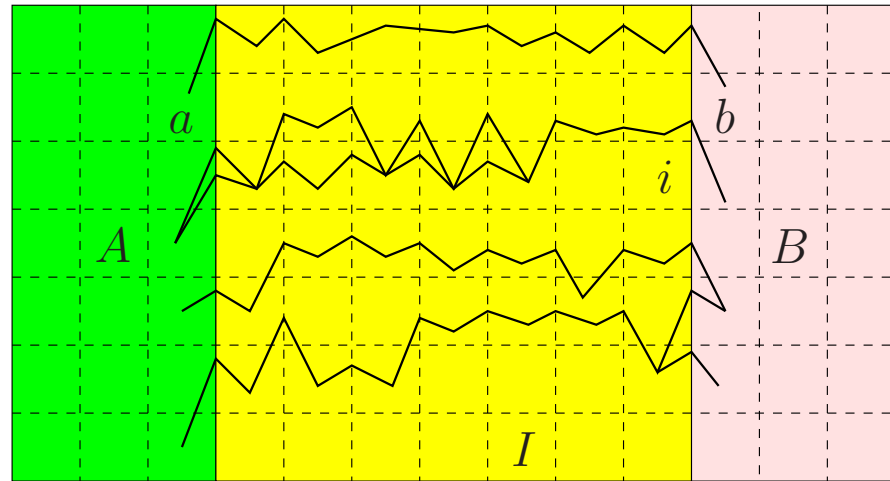
The corresponding **disconnectivity graphs** generally exhibit **funnelling** characteristics.

(*Phys. Rev. E*, **93**, 063310, 2016; *Royal Society Open Science*, **4**, 170175, 2017)

Discrete Path Sampling (*Mol. Phys.*, **100**, 3285, 2002; **102**, 891, 2004).



no intervening minima



$$\frac{p_a(t)}{p_{a'}(t)} = \frac{p_a^{\text{eq}}}{p_{a'}^{\text{eq}}} \quad \dot{p}_i(t) = 0 \quad \frac{p_b(t)}{p_{b'}(t)} = \frac{p_b^{\text{eq}}}{p_{b'}^{\text{eq}}}$$

Phenomenological $A \leftrightarrow B$ rate constants can be formulated as sums over **discrete paths**, defined as sequences of local minima and the transition states that link them, weighted by equilibrium occupation probabilities, p_b^{eq} :

$$k_{AB}^{\text{SS}} = \frac{1}{p_B^{\text{eq}}} \sum_{a \leftarrow b} P_{ai_1} P_{i_1 i_2} \cdots P_{i_{n-1} i_n} P_{i_n b} \tau_b^{-1} p_b^{\text{eq}} = \frac{1}{p_B^{\text{eq}}} \sum_{b \in B} \frac{C_b^A p_b^{\text{eq}}}{\tau_b},$$

where $P_{\alpha\beta}$ is a **branching probability** and C_b^A is the **committor** probability that the system will visit an A minimum **before** it returns to the B region.

Benchmarks for Landscape Exploration

Minimisation: Nocedal's algorithm, **LBFGS**, with line searches removed.

Transition states: single-ended searches use **hybrid eigenvector-following** (*PRB*, **59**, 3969, 1999; *JCP*, **111**, 7010, 1999; *CPL*, **341**, 185, 2001), double-ended searches use the **doubly-nudged** elastic band approach (*JCP*, **120**, 2082, 2004; **140**, 044115, 2014).

The **GMIN** (global optimisation), **OPTIM** (transition states and pathways) and **PATHSAMPLE** (discrete path sampling) programs are available from the **Cambridge Landscape Database** under the **Gnu** General Public License.

- Interfaces to many **electronic structure** codes are included.
- Current **svn** tarball image: <http://www-wales.ch.cam.ac.uk>
- <http://www-wales.ch.cam.ac.uk/tsbenchmarks.html> **Peptide** examples
- <http://theory.cm.utexas.edu/benchmarks/index.html> **OptBench** test suite
- <https://github.com/wales-group/examples> **Curated examples**

A Knotted Protein (*PLoS Comput. Biol.*, **6**, e1000835, 2010)

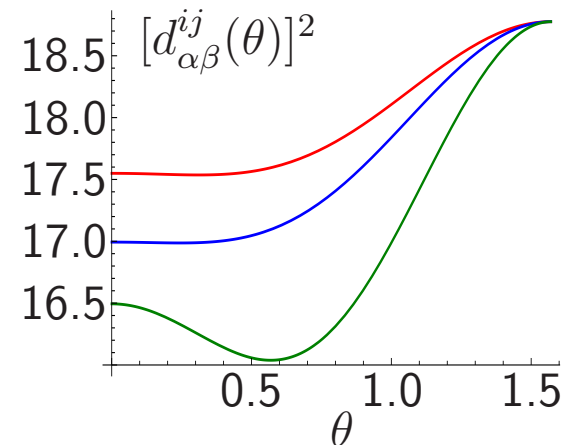
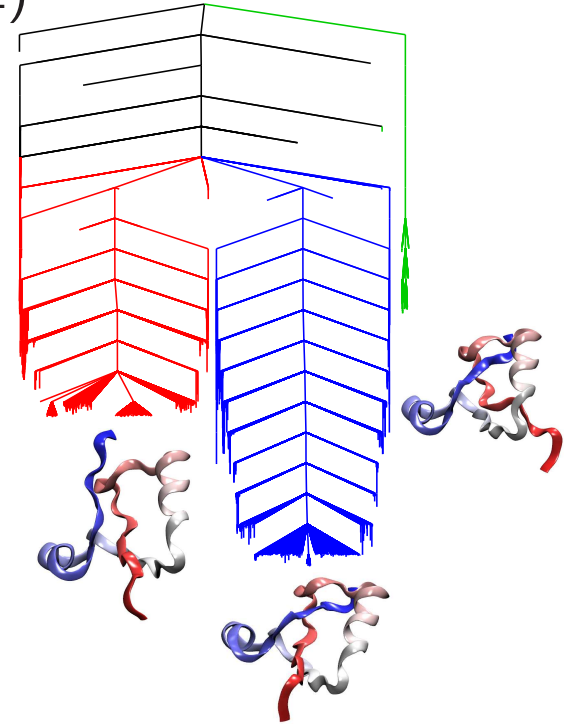
Quasi-Continuous Interpolation (*JCTC*, **8**, 5020, 2012)

The tRNA methyltransferase protein 1UAM contains a deep **trefoil knot** (right).

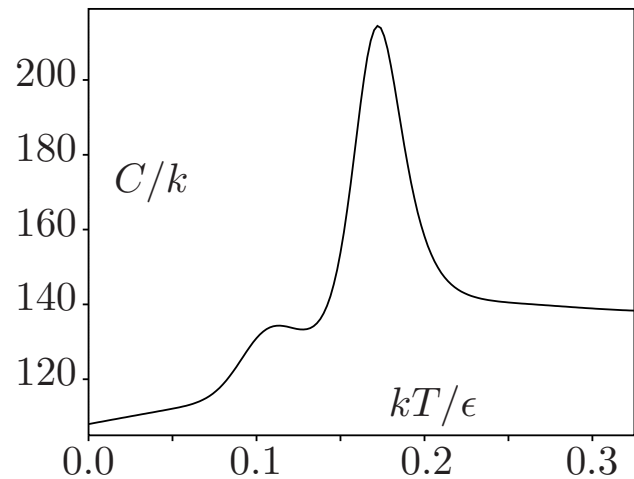
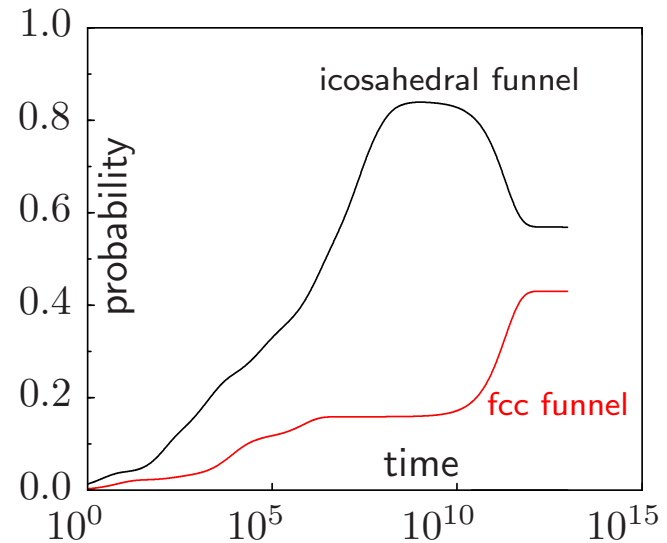
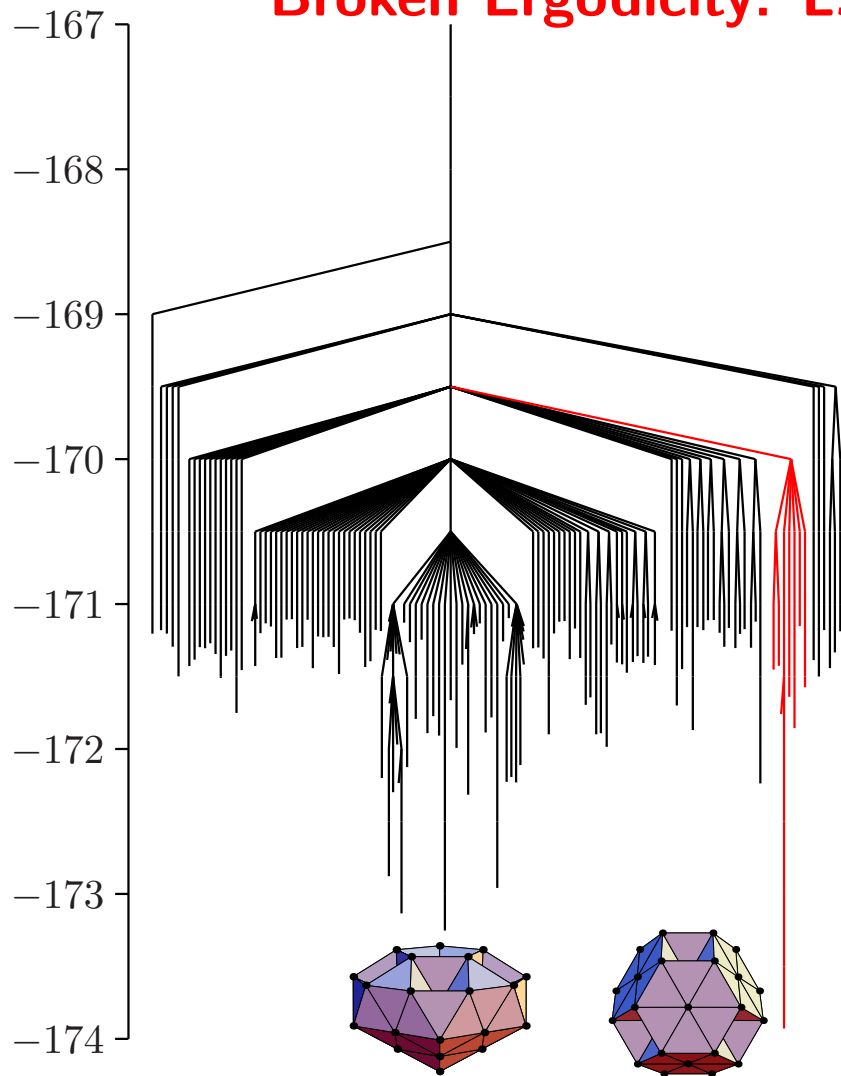
The folding pathway exhibits two **slipknot**-type steps for a truncated (residues 78–135) **Gō model** using an **associated memory Hamiltonian** and initial **QCI**.

The **QCI** potential **preserves** the covalent bonding framework, with short-range **repulsion** between **unconstrained** atoms. An **internal** minimum for **atoms** α and β between **images** i and j occurs at

$$[d_{\alpha\beta}^{ij}(\theta)]^2 = \frac{|\mathbf{r}_{\alpha}^i - \mathbf{r}_{\beta}^i|^2 |\mathbf{r}_{\alpha}^j - \mathbf{r}_{\beta}^j|^2 - [(\mathbf{r}_{\alpha}^i - \mathbf{r}_{\beta}^i) \cdot (\mathbf{r}_{\alpha}^j - \mathbf{r}_{\beta}^j)]^2}{|\mathbf{r}_{\alpha}^i - \mathbf{r}_{\beta}^i - \mathbf{r}_{\alpha}^j + \mathbf{r}_{\beta}^j|^2}.$$



Broken Ergodicity: LJ_{38} (*Phys. Rev. E*, **60**, 3701, 1999)



LJ_{38} exhibits a **double funnel** due to competition between icosahedral and truncated **octahedral** morphologies. The interconversion rate for Ar_{38} is calculated as 55 s^{-1} at 14 K where a **solid-solid** transition occurs.

Simulating structural transitions by direct transition current sampling: The example of LJ₃₈

Massimiliano Picciani,^{1,a)} Manuel Athènes,¹ Jorge Kurchan,² and Julien Tailleur³

¹*CEA, DEN, Service de Recherches de Métallurgie Physique, F-91191 Gif-sur-Yvette, France*

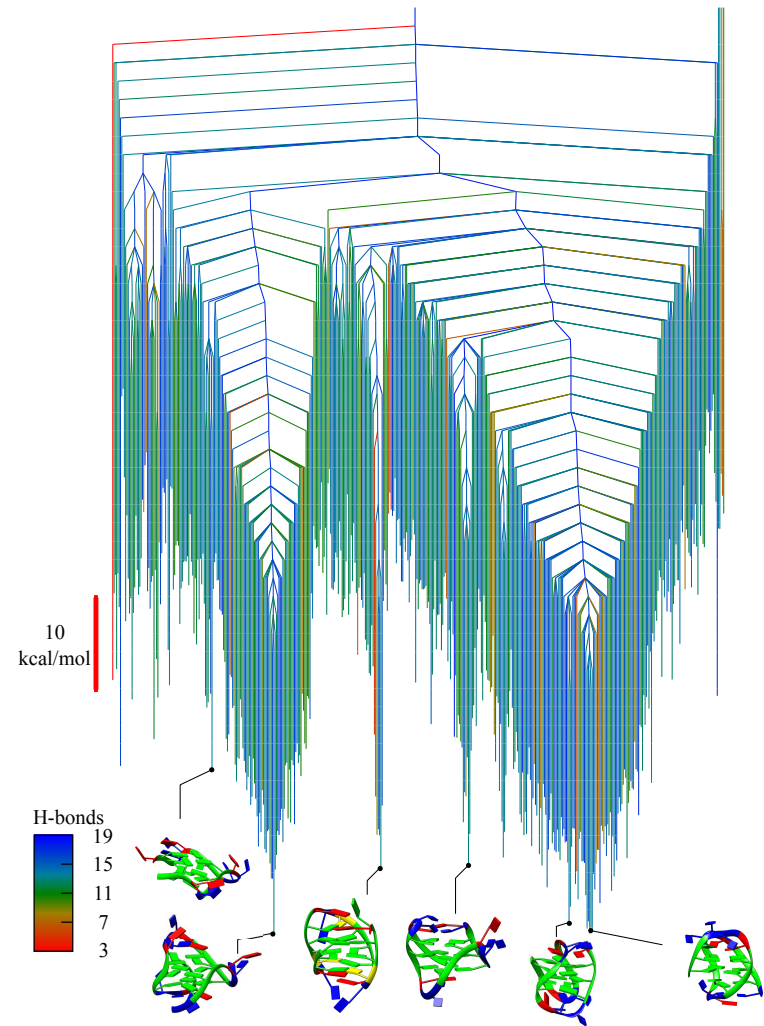
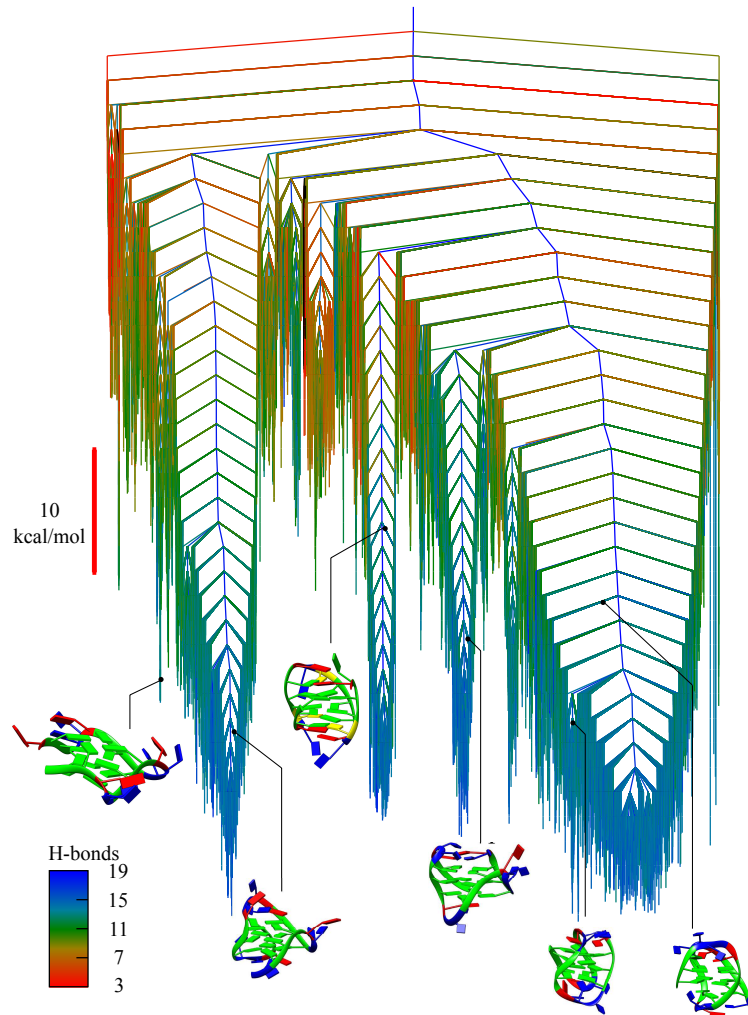
²*CNRS; ESPCI, 10 rue Vauquelin, UMR 7636 PMMH, 75005 Paris, France*

³*School of Physics of Astronomy, SUPA, University of Edinburgh, The King's Buildings, Mayfield Road, EH9 3JZ Edinburgh, United Kingdom*

(Received 2 March 2011; accepted 21 June 2011; published online 20 July 2011)

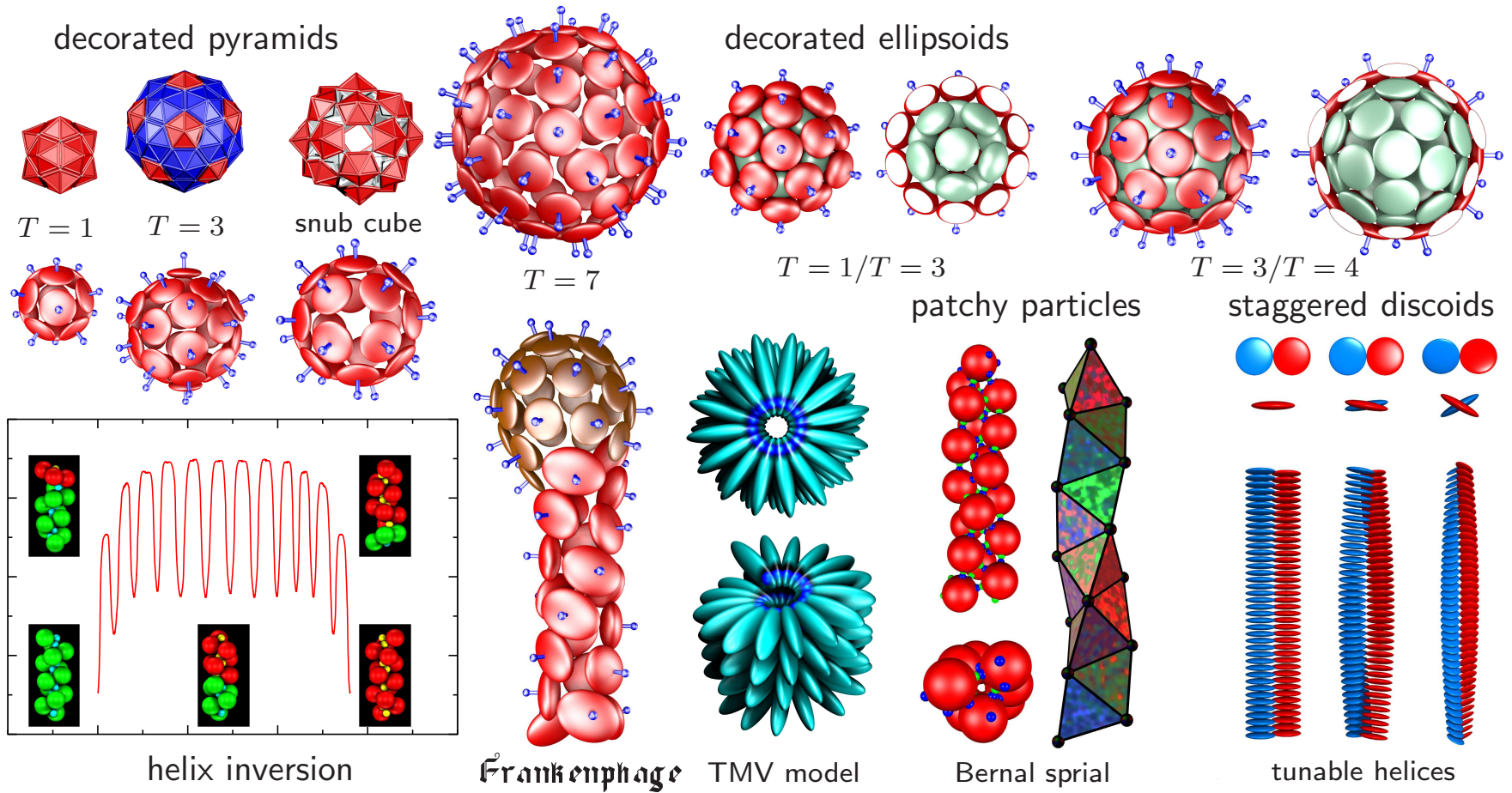
Another attempt to study the transitions between the two funnels of LJ₃₈ relies on the use of transition path sampling.³³ Because of the number of metastable states separating the two main basins, the traditional shooting and shifting algorithm failed here, despite previous success for smaller LJ clusters.³⁹ The authors thus developed a two-ended approach which manages to successfully locate reaction paths between the two basins: they started from a straight trial trajectory linking the two minima, and obtained convergence towards trajectories of energies similar to those obtained in the discrete path sampling approach.³³ Although the authors point out the lack of ergodicity in the sampling within their approach and the sensitivity on the “discretization” of the trajectories, this is nevertheless a progress and the main drawback remains the high computational cost (the work needed 10^5 h of central processing unit (cpu) time) to obtain such converged trajectories. In contrast, the simulations we present below required less than 10^2 h of cpu time.

Landscapes for a DNA four-fold telomere repeat: $A(G_3TTA)_3G_3$



G-quadruplexes, stabilised by **quartets** of **guanine** bases, decrease the activity of **telomerase**, which maintains the **length** of telomeric repeats. **Misfunctioning** is associated with numerous **cancer** conditions. (*JCP*, **147**, 152715, 2017)

Coarse-Grained Models (*PCCP*, 11, 1970, 2009; *ACS Nano*, 4, 219, 2010)



The **angle-axis** formulation provides a particularly convenient framework for **mesoscopic** modelling, using both **decorated** rigid bodies and **ellipsoids**.

All the terms involving **angle-axis** coordinates can be obtained by the action of a **rotation matrix** and its derivatives, which are **system-independent**.

1st derivatives: $\mathbf{R}_k \equiv \frac{\partial \mathbf{R}}{\partial p_k} = \frac{p_k \sin \theta}{\theta} \tilde{\mathbf{p}}^2 + (1 - \cos \theta)(\tilde{\mathbf{p}}_k \tilde{\mathbf{p}} + \tilde{\mathbf{p}} \tilde{\mathbf{p}}_k) + \frac{p_k \cos \theta}{\theta} \tilde{\mathbf{p}} + \sin \theta \tilde{\mathbf{p}}_k$, with $\tilde{\mathbf{p}}_1 = \frac{1}{\theta^3} \begin{pmatrix} 0 & p_1 p_3 & -p_1 p_2 \\ -p_1 p_3 & 0 & p_1^2 - \theta^2 \\ p_1 p_2 & \theta^2 - p_1^2 & 0 \end{pmatrix}$

2nd derivatives: $\mathbf{R}_{kk} \equiv \frac{\partial^2 \mathbf{R}}{\partial p_k^2} = \frac{2p_k \sin \theta}{\theta} (\tilde{\mathbf{p}}_k \tilde{\mathbf{p}} + \tilde{\mathbf{p}} \tilde{\mathbf{p}}_k) + \left(\frac{p_k^2 \cos \theta}{\theta^2} - \frac{p_k^2 \sin \theta}{\theta^3} + \frac{\sin \theta}{\theta} \right) \tilde{\mathbf{p}}^2$
 $+ (1 - \cos \theta)(2\tilde{\mathbf{p}}_k^2 + \tilde{\mathbf{p}}_{kk} \tilde{\mathbf{p}} + \tilde{\mathbf{p}} \tilde{\mathbf{p}}_{kk}) + \left(-\frac{p_k^2 \sin \theta}{\theta^2} - \frac{p_k^2 \cos \theta}{\theta^3} + \frac{\cos \theta}{\theta} \right) \tilde{\mathbf{p}} + \frac{2p_k \cos \theta}{\theta} \tilde{\mathbf{p}}_k + \sin \theta \tilde{\mathbf{p}}_{kk}$,

and $\mathbf{R}_{kl} \equiv \frac{\partial^2 \mathbf{R}}{\partial p_k \partial p_l} = \frac{p_k \sin \theta}{\theta} (\tilde{\mathbf{p}}_l \tilde{\mathbf{p}} + \tilde{\mathbf{p}} \tilde{\mathbf{p}}_l) + \left(\frac{p_k p_l \cos \theta}{\theta^2} - \frac{p_k p_l \sin \theta}{\theta^3} \right) \tilde{\mathbf{p}}^2 + \frac{p_l \sin \theta}{\theta} (\tilde{\mathbf{p}}_k \tilde{\mathbf{p}} + \tilde{\mathbf{p}} \tilde{\mathbf{p}}_k)$
 $+ (1 - \cos \theta)(\tilde{\mathbf{p}}_{kl} \tilde{\mathbf{p}} + \tilde{\mathbf{p}}_k \tilde{\mathbf{p}}_l + \tilde{\mathbf{p}}_l \tilde{\mathbf{p}}_k + \tilde{\mathbf{p}} \tilde{\mathbf{p}}_{kl}) - \left(\frac{p_k p_l \sin \theta}{\theta^2} + \frac{p_k p_l \cos \theta}{\theta^3} \right) \tilde{\mathbf{p}} + \frac{p_k \cos \theta}{\theta} \tilde{\mathbf{p}}_l + \frac{p_l \cos \theta}{\theta} \tilde{\mathbf{p}}_k + \sin \theta \tilde{\mathbf{p}}_{kl}$.

Denote positions in the **body-fixed** frame by superscript 0. For rigid bodies I and J with sites i and j defining site-site **isotropic** potentials U_{ij}^{IJ} the **potential energy** is

$$U = \sum_I \sum_{J < I} \sum_{i \in I} \sum_{j \in J} f_{ij}(r_{ij}), \quad \text{where} \quad r_{ij} = |\mathbf{r}_{ij}| = |\mathbf{r}_i - \mathbf{r}_j| \quad \text{and} \quad f_{ij} \equiv U_{ij}^{IJ} \quad \text{so that}$$

$$\frac{\partial U}{\partial \zeta} = \sum_{J \neq I} \sum_{i \in I} \sum_{j \in J} f'_{ij}(r_{ij}) \frac{\partial r_{ij}}{\partial \zeta}, \quad \text{where} \quad f'_{ij} = \frac{df_{ij}(r_{ij})}{dr_{ij}}, \quad \frac{\partial r_{ij}}{\partial \mathbf{r}^I} = \hat{\mathbf{r}}_{ij}, \quad \frac{\partial r_{ij}}{\partial p_k^I} = \hat{\mathbf{r}}_{ij} \cdot \frac{\partial \mathbf{r}_{ij}}{\partial p_k^I} = \hat{\mathbf{r}}_{ij} \cdot (\mathbf{R}_k^I \mathbf{r}_i^0), \quad \mathbf{r}_{ij} = \mathbf{r}^I + \mathbf{R}^I \mathbf{r}_i^0 - \mathbf{r}^J - \mathbf{R}^J \mathbf{r}_j^0.$$

$$\frac{\partial^2 U_{ij}^{IJ}}{\partial r_k^I \partial r_l^J} = f_2(r_{ij}) r_{ij,k} r_{ij,l} \epsilon_{IJ} + f_1(r_{ij}) \delta_{kl} \epsilon_{IJ},$$

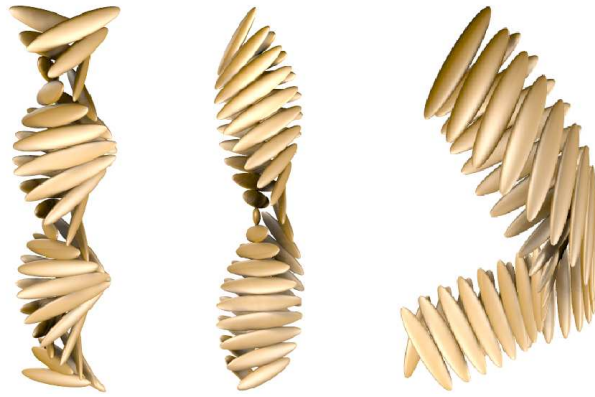
$$\frac{\partial^2 U_{ij}^{IJ}}{\partial p_k^I \partial p_l^J} = f_2(r_{ij}) (\mathbf{r}_{ij} \cdot \mathbf{R}_k^I \mathbf{r}_i^0) (\mathbf{r}_{ij} \cdot \mathbf{R}_l^J \mathbf{r}_j^0) \delta_{IJ} - f_2(r_{ij}) (\mathbf{r}_{ij} \cdot \mathbf{R}_k^I \mathbf{r}_i^0) (\mathbf{r}_{ij} \cdot \mathbf{R}_l^J \mathbf{r}_j^0) (1 - \delta_{IJ}) + f_1(r_{ij}) (\mathbf{R}_k^I \mathbf{r}_i^0) \cdot (\mathbf{R}_l^J \mathbf{r}_j^0) \delta_{IJ}$$

$$- f_1(r_{ij}) (\mathbf{R}_k^I \mathbf{r}_i^0) \cdot (\mathbf{R}_l^J \mathbf{r}_j^0) (1 - \delta_{IJ}) + f_1(r_{ij}) (\mathbf{r}_{ij} \cdot \mathbf{R}_{kl}^I \mathbf{r}_i^0) \delta_{IJ},$$

$$\frac{\partial^2 U_{ij}^{IJ}}{\partial r_k^I \partial p_l^J} = f_2(r_{ij}) (\mathbf{r}_{ij} \cdot \mathbf{R}_l^J \mathbf{r}_j^0) r_{ij,k} \delta_{IJ} - f_2(r_{ij}) (\mathbf{r}_{ij} \cdot \mathbf{R}_l^J \mathbf{r}_j^0) r_{ij,k} (1 - \delta_{IJ}) + f_1(r_{ij}) [\mathbf{R}_k^I \mathbf{r}_i^0]_l \delta_{IJ} - f_1(r_{ij}) [\mathbf{R}_l^J \mathbf{r}_j^0]_l (1 - \delta_{IJ}).$$

where $f_1(r_{ij}) = f'_{ij}(r_{ij})/r_{ij}$, $f_2(r_{ij}) = f''_{ij}(r_{ij})/r_{ij}$, $\epsilon_{IJ} = 1$ for $I = J$ and $\epsilon_{IJ} = -1$ for $I \neq J$, and δ_{IJ} is the Kronecker delta.

Helical Bilayers From Frustrated Building Blocks (*JPCB*, 117, 7918, 2013)



helical fibre morphologies

bilayer filaments

magnetic bilayers

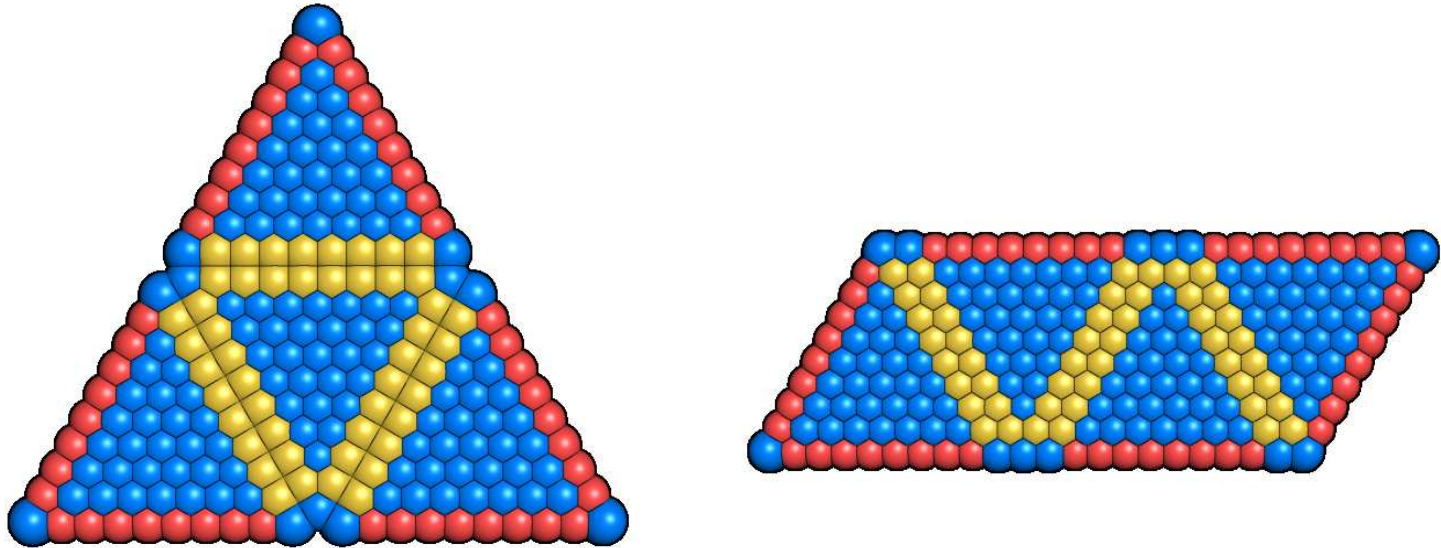
Left: introduction of a **cytochrome** domain into an **amyloid fibre** can change the morphology from **twisted** to **spiral** ribbons and induce systematic **kinking**.

Centre: rigid building blocks consisting of **two ellipsoids** can reproduce these structures, which are also observed for **Bauhinia seedpods**.

Right: the structure depends mostly on the **internal geometry** of the building blocks, rather than details of the **potential**. The **design** principles extend to **macroscopic** helices formed from elliptical **magnets**.

Polyhedral Nets

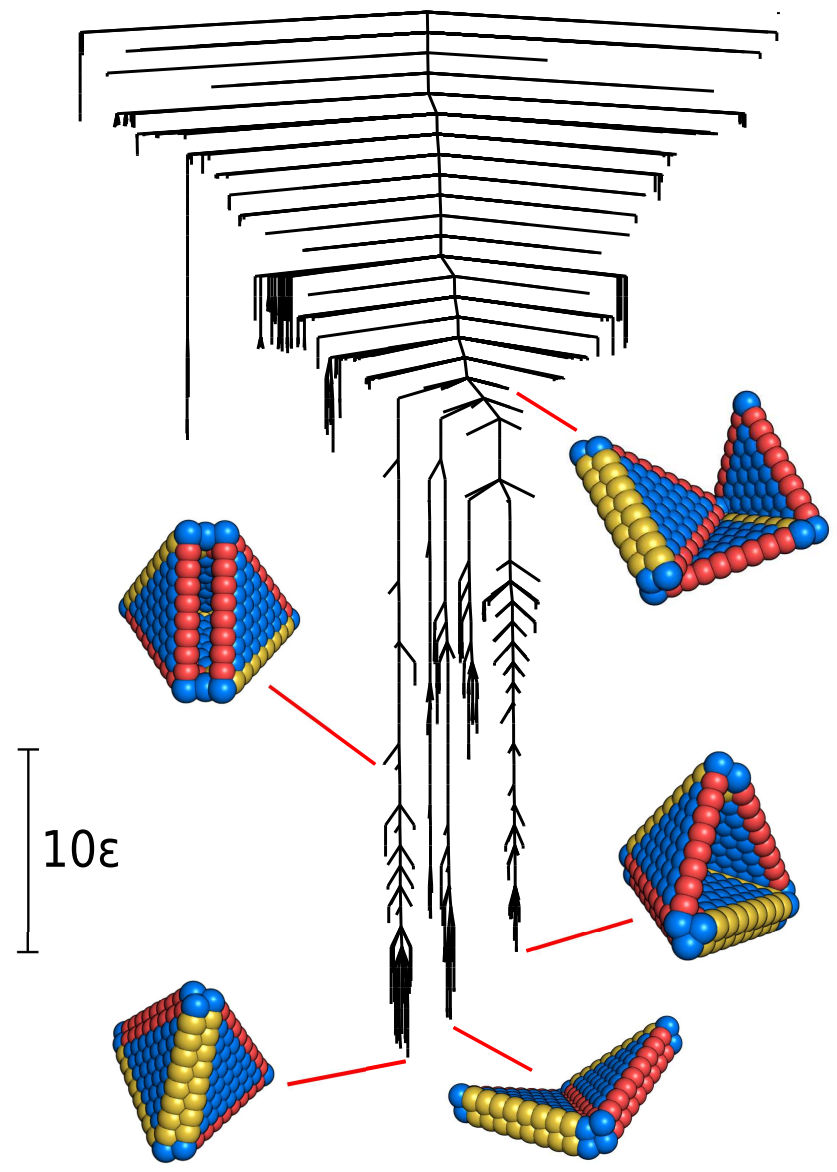
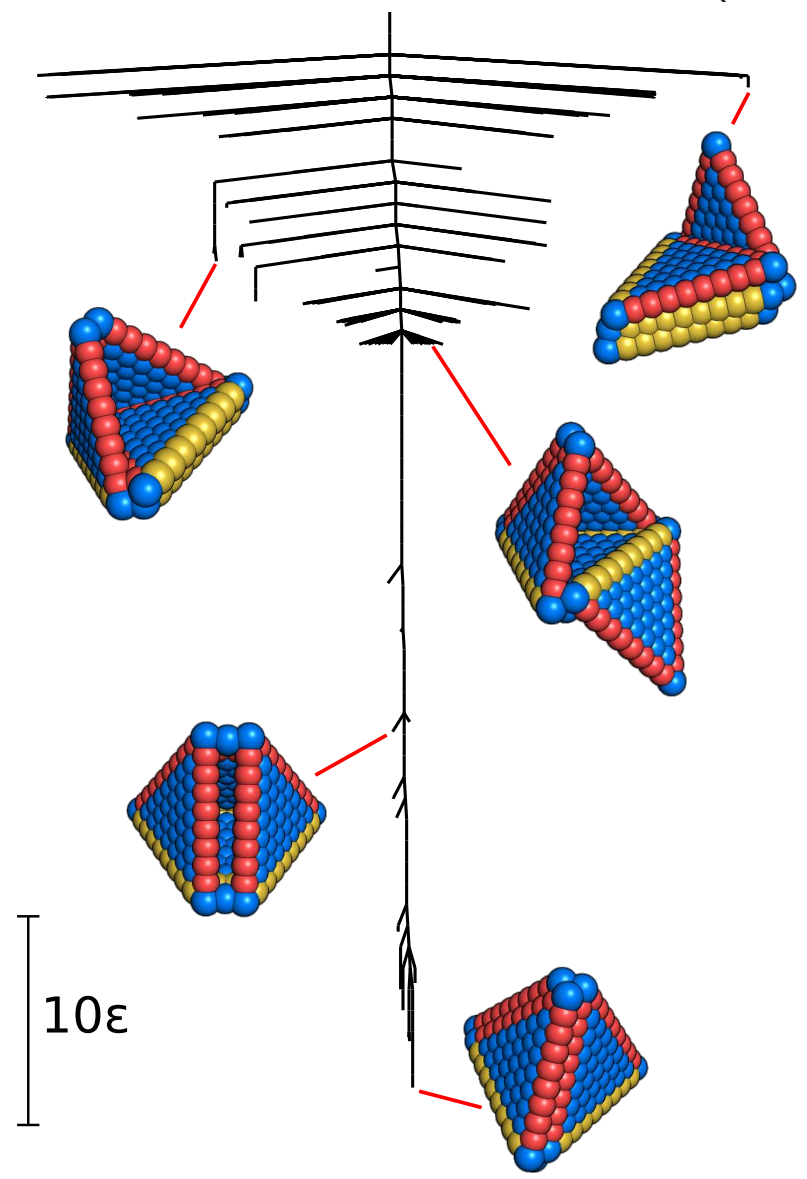
Successful **self-assembly** of 200 and 500 μm **cubes** and **octahedra** from tethered, multi-component nets was found to correlate with **compactness**.



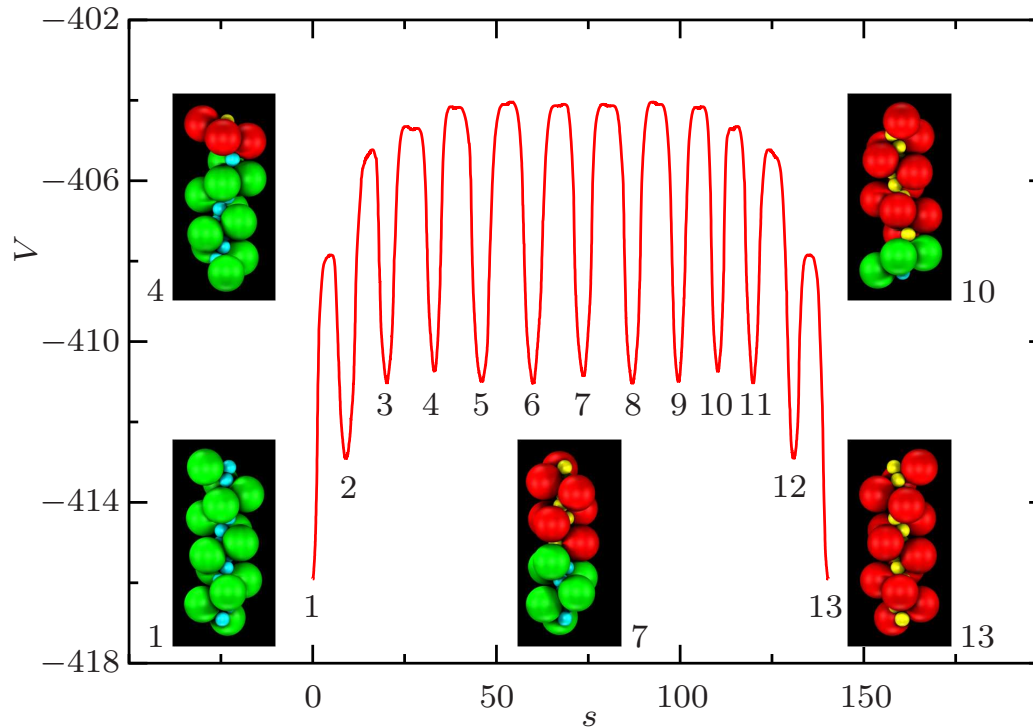
Models for **tetrahedra** developed by Glotzer et al. are based on:

- **Repulsive** interior sites - Weeks-Chandler-Andersen potential
- **Sticky** sites along free edges - Lennard-Jones potential
- **Stiff harmonic springs** along fixed edges

Self-assembly of a **tetrahedron** is more efficient for the **triangular** net (left) than the **frustrated linear** net (right).



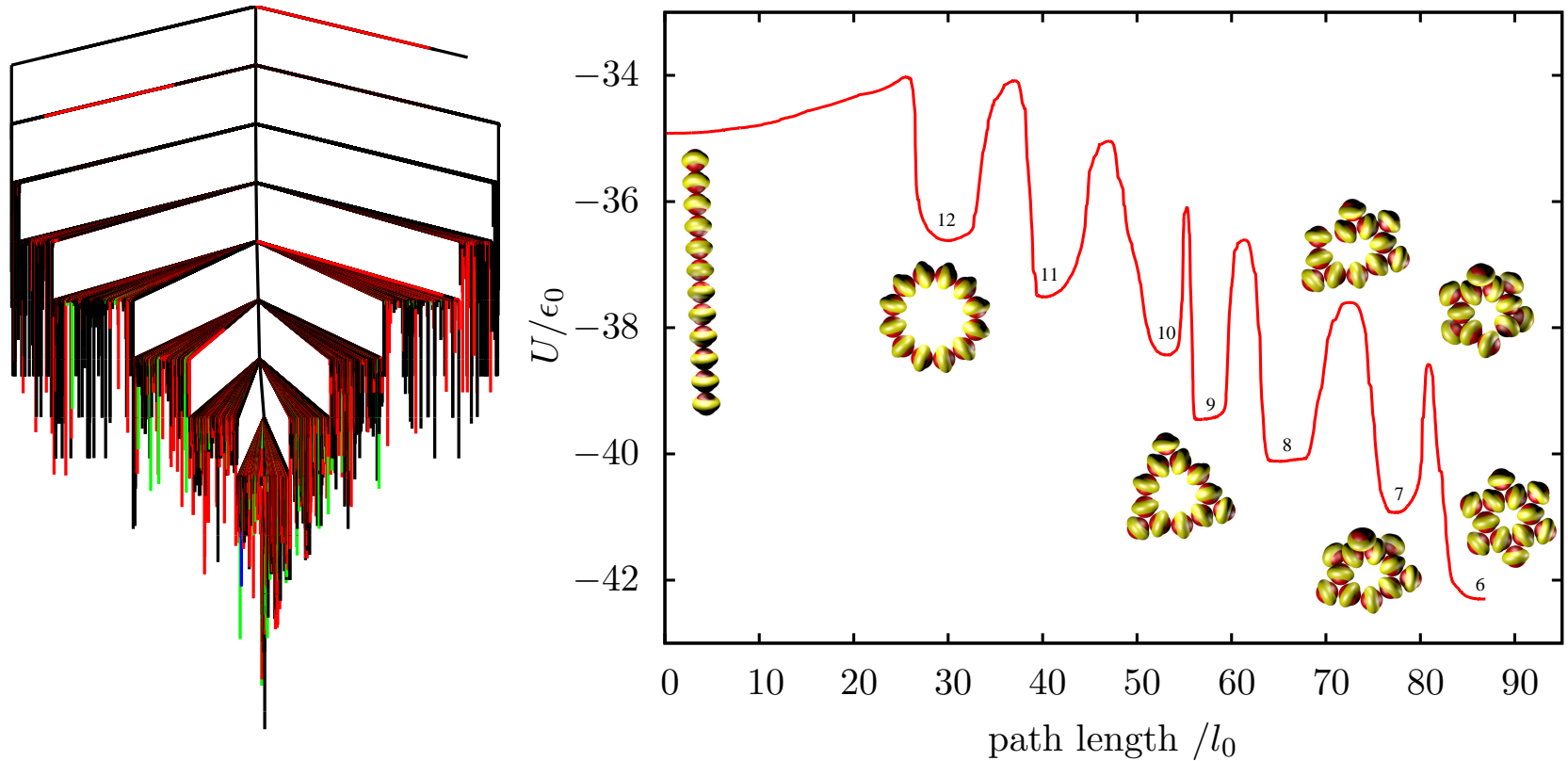
A Nanodevice (*Soft Matter*, 7, 2325, 2011)




Coupled **linear** and **rotary** motion has been characterised for a helix composed of 13 asymmetric **dipolar dumbbells** in the presence of an **electric field**.

The helix changes **handedness** as the boundary between segments propagates along the strand via successive steps that switch the dumbbells.

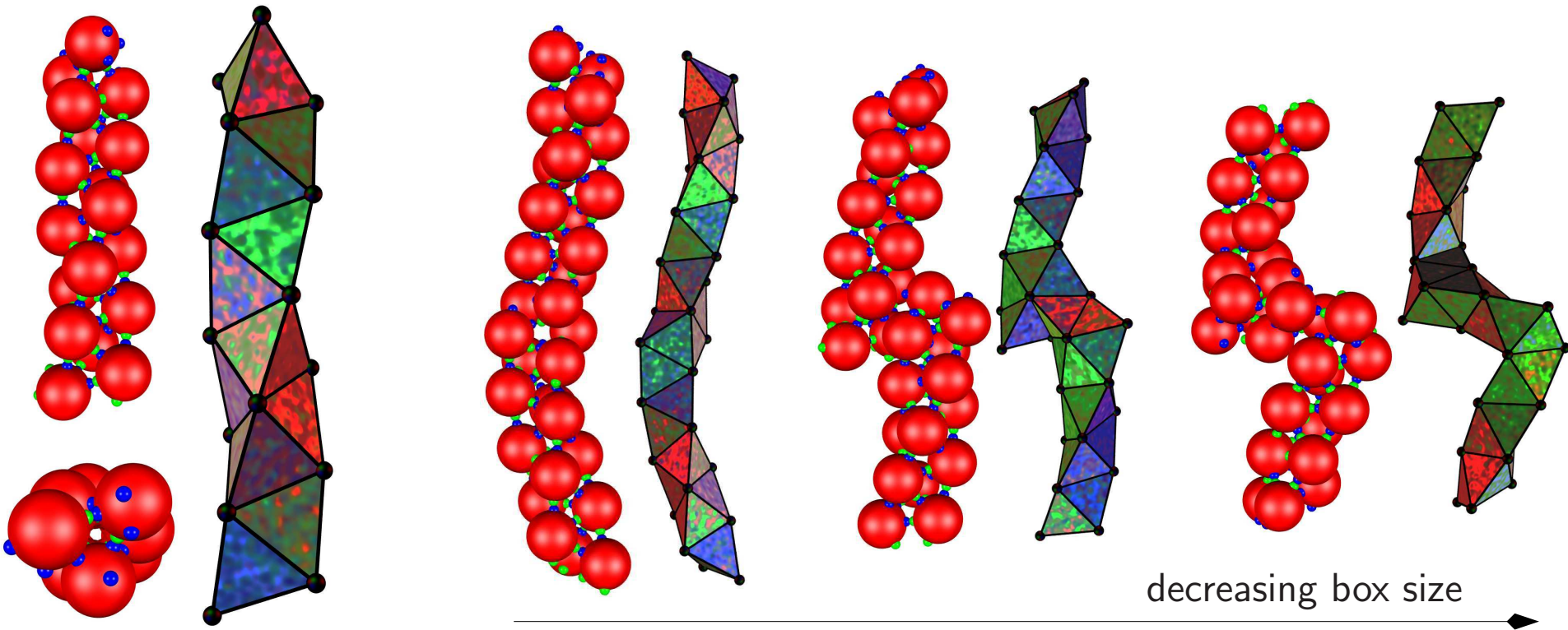
Kagome Structures (Soft Matter, 11, 6663, 2015)



Energetically stabilised **Kagome** structures were designed using soft anisotropic triblock **Janus** particles.  This **unconstrained** model predicts that **sedimentation** effects **enhance** the stability.

Rearrangements between competing structures are highly **cooperative**.

Designing a Bernal Spiral (ACS Nano, 7, 1246, 2013)

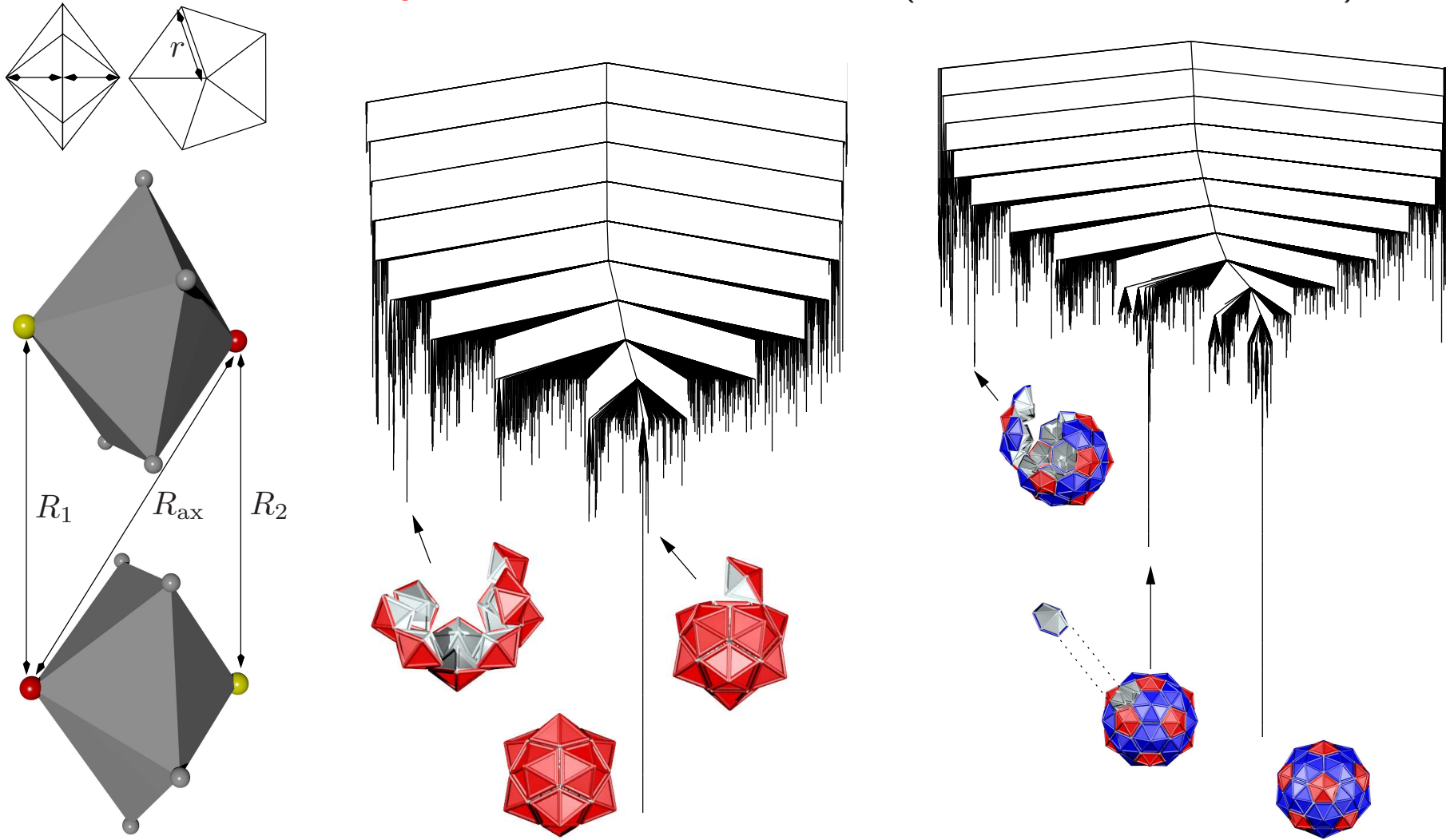


The simplest building blocks that support a Bernal spiral as the global minimum involve a **single** patch-antipatch pair **offset** by about 10° from linearity.

Left: Alternative views of a chiral Bernal spiral consisting of 18 particles.

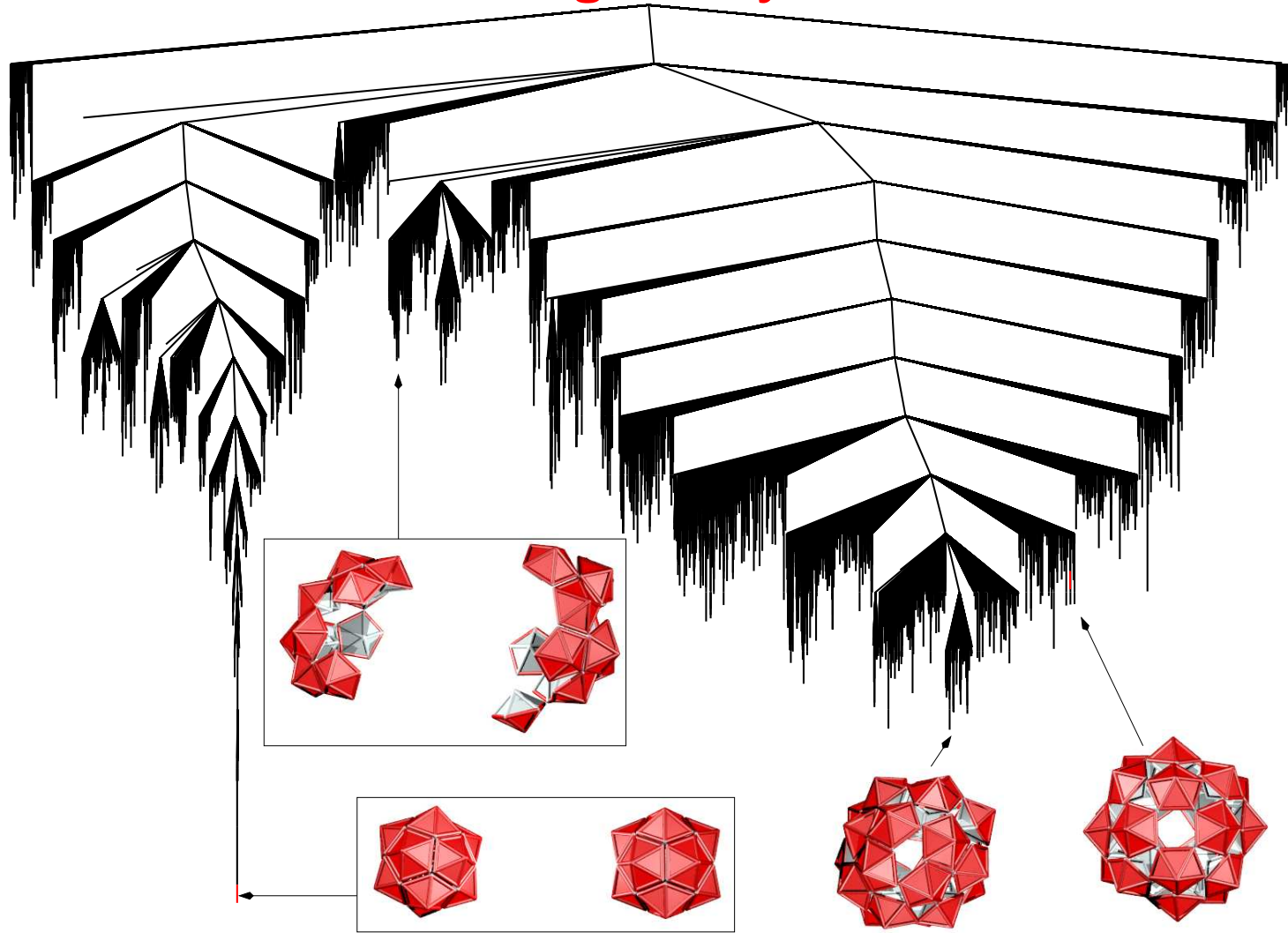
Right: **compressed** spirals (30 particles, periodic boundaries) exhibit **supercoiling** or **breaks**, which resemble structures seen in **confocal microscopy**.

Self-Assembly of Icosahedral Shells (*PCCP*, 11, 2098-2104, 2009)



Palm tree disconnectivity graphs with I_h global minima are found for $T = 1$ and $T = 3$ shells constructed from **pentagonal** and **hexagonal** pyramids. These **landscapes** correspond to efficient **self-organisation**.

24 Pentagonal Pyramids

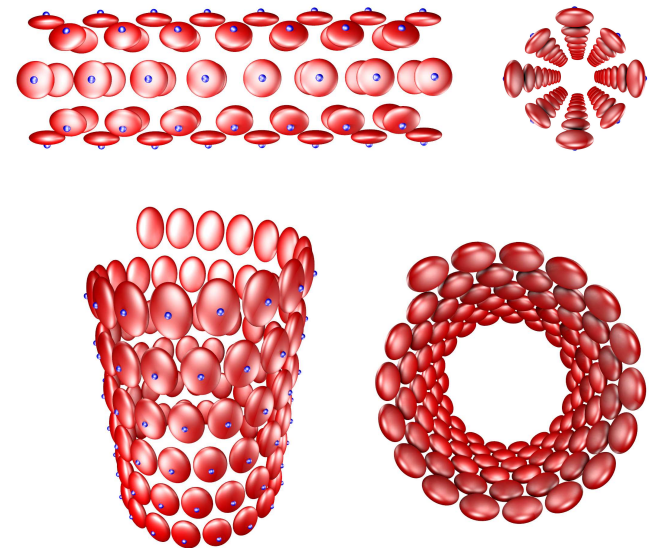
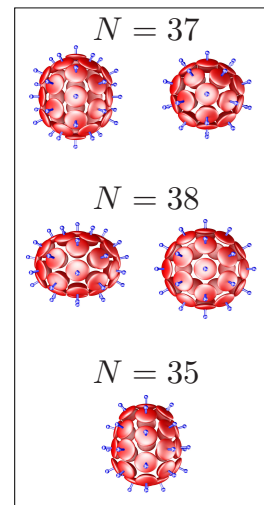
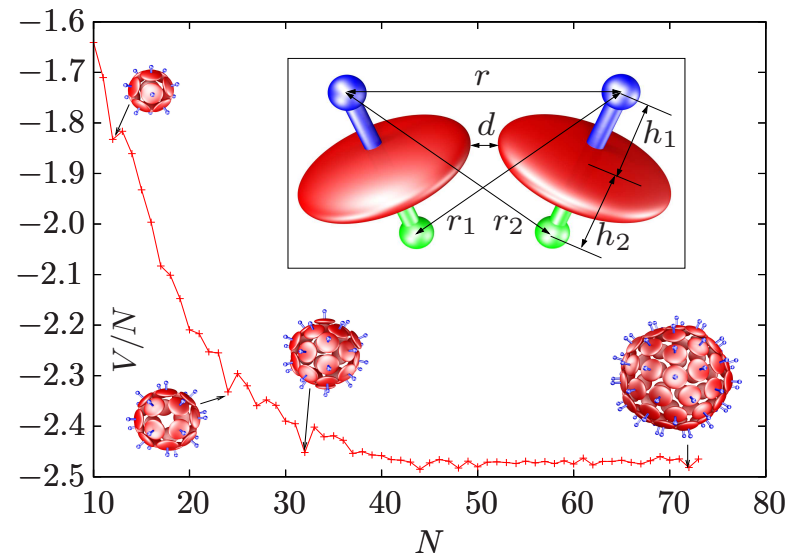


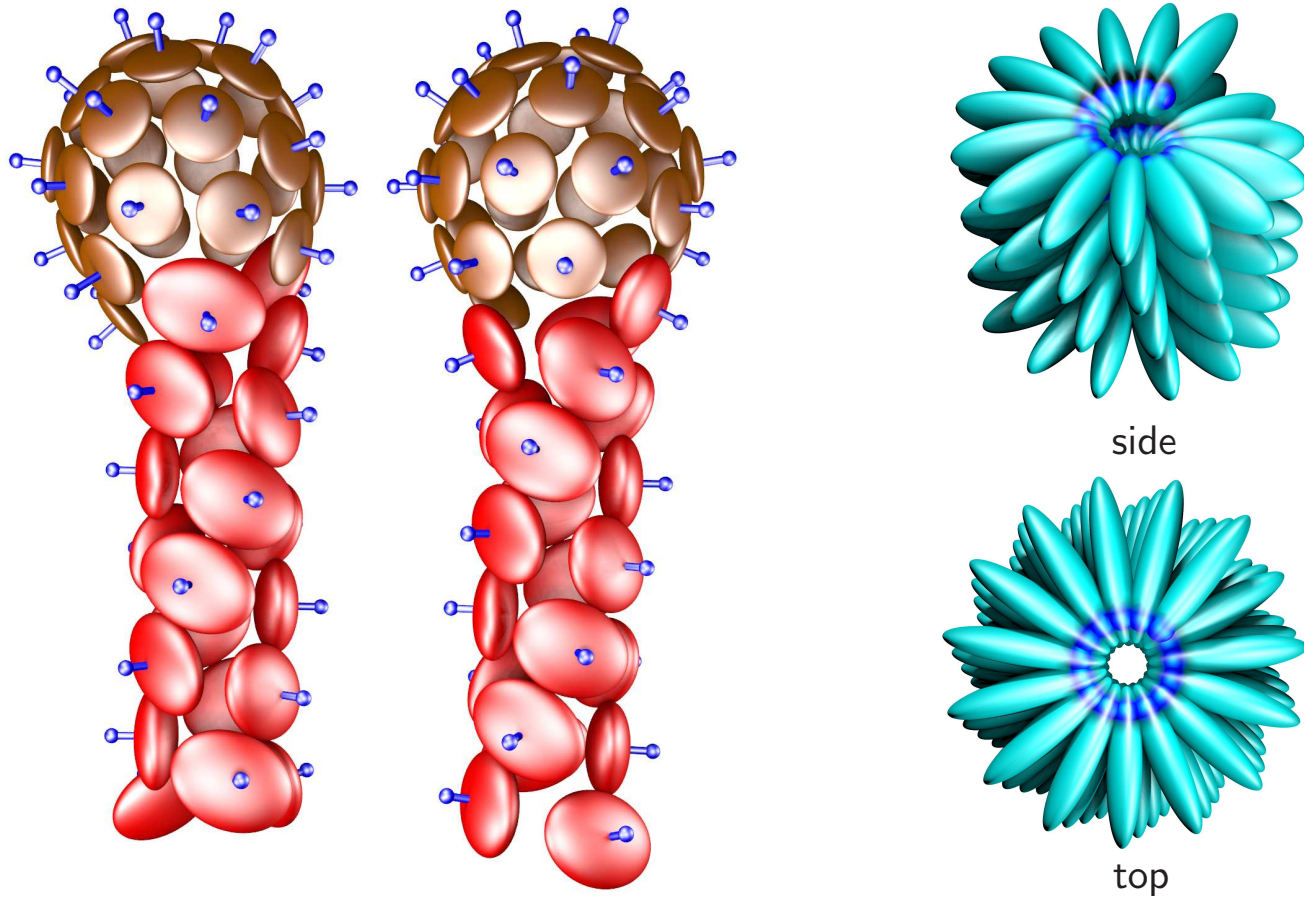
For the same parameters two $T = 1$ **icosahedra** are similar in energy to a **single shell** based on a **snub cube**. *Polyoma virus* capsid protein VP₁ forms a left-handed **snub cube** from alkaline solution in the absence of the genome.

Emergent Behaviour from Simple Models (*ACS Nano*, 4, 219, 2010)

Adding two repulsive **axial** Lennard-Jones sites to an **ellipsoidal** core produces remarkably versatile building blocks. **Oblate** ellipsoids favour **shells**, while stronger repulsion for the longer semiaxis produces **tubes** and **spirals**.

Global minima for the **oblate** ellipsoids include **icosahedra** for $N = 12, 32$ and 72 ($T = 1, 3$ and 7), the **snub cube** observed for polyoma virus capsids at $N = 24$, and **conical**, **biaxial**, **prolate**, and **oblate** shells at other sizes.





Mixing ellipsoidal building blocks that favour shells and tubes produces structures with distinct **head** and **tail** regions (left): the **Frankenphage**.

Particles with a Lennard-Jones site **buried** in the ellipsoid assemble into a **spiral** structure (right) with parameters similar to **tobacco mosaic virus**.

Connecting Dynamics and Thermodynamics (*Science*, 293, 2067, 2001)

The organisation of a PES is governed by its **stationary points**, where Taylor expansions provide local descriptions in terms of **Hessian matrices**.

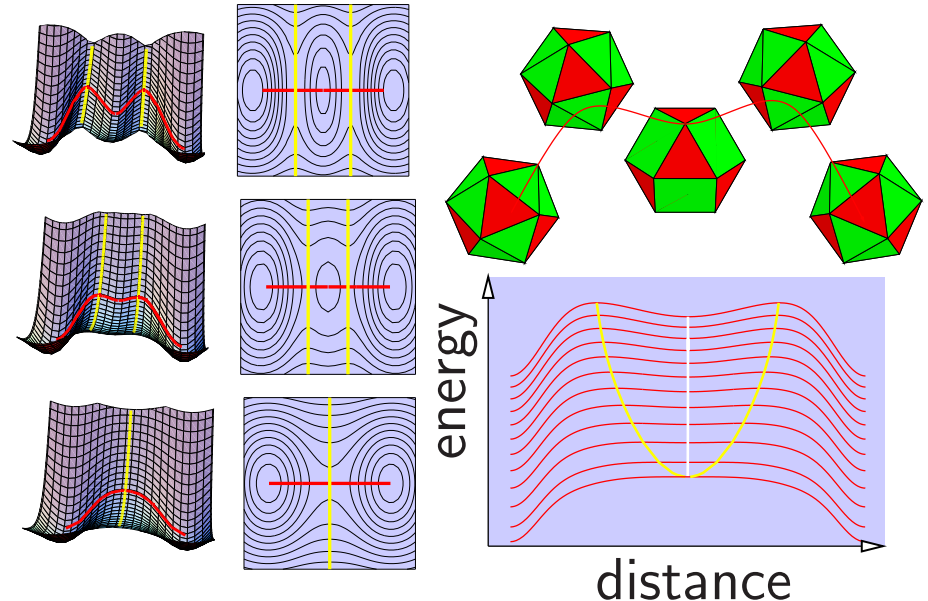
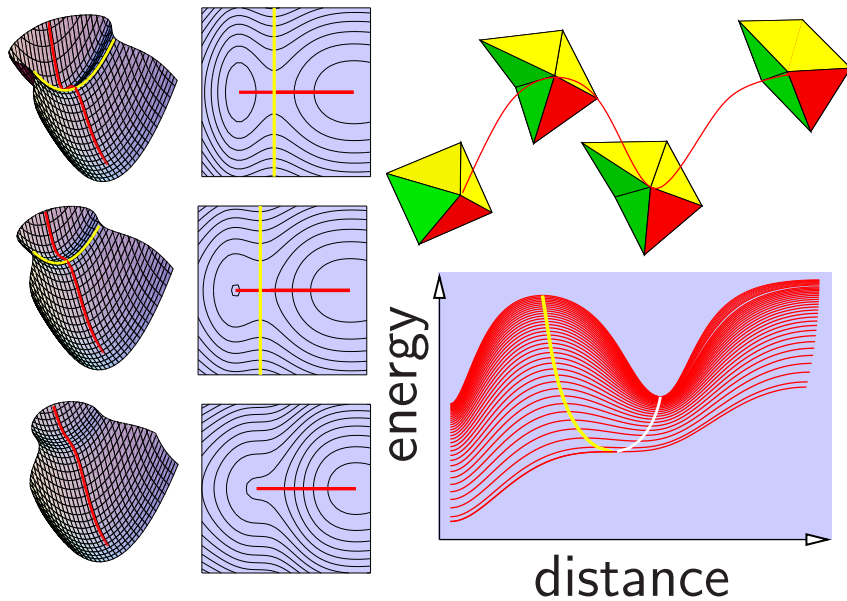
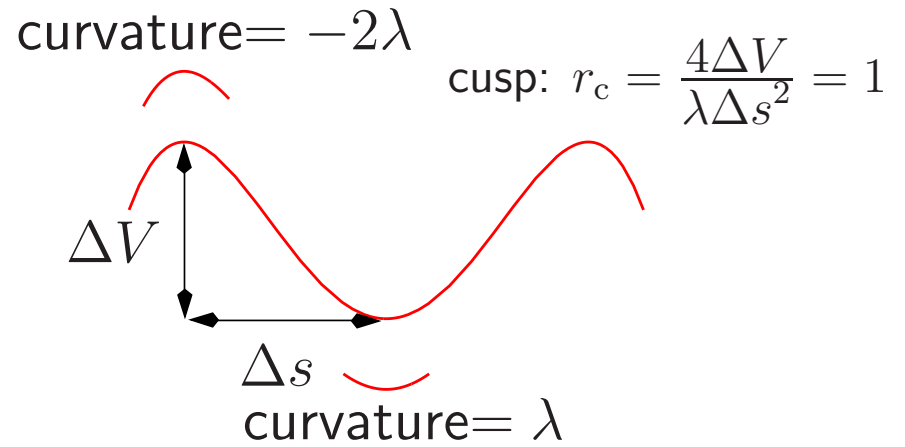
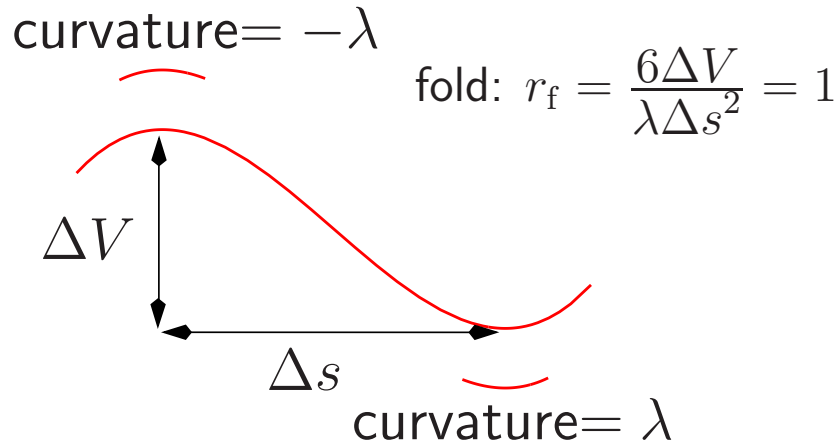
The organisation of **families** of PES's as a function of **parameters** in the potential is determined by the stationary points that possess additional zero Hessian eigenvalues, known as **non-Morse** points.

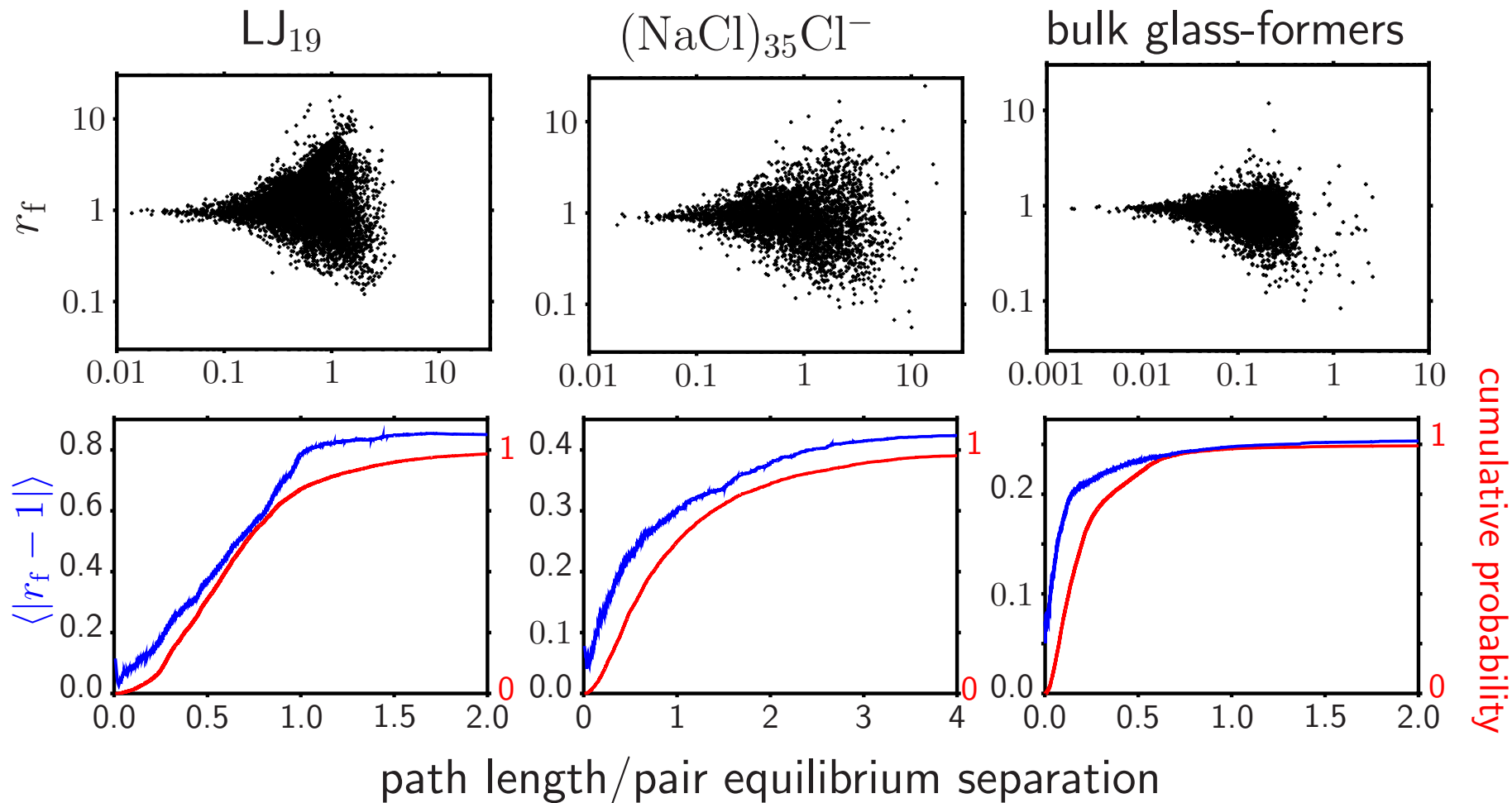
Catastrophe theory provides a local representation of the PES around non-Morse points as a function of **both** atomic coordinates and parameters.

The **splitting lemma** reduces the dimensionality to the **essential** variables, while **transversality** guarantees that the resulting classifications are **universal**.

The simplest one-parameter catastrophes are the **fold**, $f(x) = \frac{1}{3}x^3 + ax$, and the symmetrical **cusp**, $f(x) = \frac{1}{4}x^4 + \frac{1}{2}ax^2$.

Geometries of the **fold** and **cusp** catastrophes.





For systems with a fixed potential we effectively have a **snap-shot** of parameter space. On average, r_f remains **close to unity** for many pathways in both model clusters and bulk, providing an explanation for **Hammond's postulate**.